Intellectual disability-associated SMARCB1 mutations reveal a nucleosome acidic patch interaction site that potentiates mSWI/SNF chromatin remodeling

Alfredo M. Valencia[1,2,3], **Clayton K. Collings**[1,2], **Hai T. Dao**[4], **Roodolph St. Pierre**[1,2,3], **Yung-Chih Cheng**[5,6,7], **Junwei Huang**[5,6,7], **Zhen-Yu Sun**[8,9], **Hyuk-Soo Seo**[8,9], **Nazar Mashtalir**[1,2], **Dawn E. Comstock**[1,2,10], **Olubusayo Bolonduro**[1,2], **Nicholas E. Vangos**[8,9], **Zoe C. Yeoh**[8,9], **Mary Kate Dornon**[5,6,7], **Crystal Hermawan**[5,6,7], **Lee Barrett**[5,6,7], **Sirano Dhe-Paganon**[8], **Clifford J. Woolf**[5,6,7], **Tom W. Muir**[4], **Cigall Kadoch**[1,2,11,*]

[1]Department of Pediatric Oncology, Dana-Farber Cancer Institute and Harvard Medical School, Boston, MA 02215 USA

[2]Broad Institute of MIT and Harvard, Cambridge, MA 02142 USA

[3]Chemical Biology Program, Harvard University, Cambridge MA 02138 USA

[4]Department of Chemistry, Princeton University, Princeton NJ 08544 USA

[5]F.M. Kirby Neurobiology Center, Boston Children's Hospital, Boston, MA 02115 USA

[6]Department of Neurobiology, Harvard Medical School, Boston, MA 02115 USA

[7]Harvard Stem Cell Institute, Cambridge, MA 02138 USA

[8]Department of Cancer Biology, Dana-Farber Cancer Institute, Boston, MA 02215 USA

[9]Department of Biological Chemistry & Molecular Pharmacology, Harvard Medical School, Boston, MA 02115 USA

[10]Program in Immunology, Harvard Medical School, Boston, MA 02115 USA

[11]Lead Contact

Abstract

Mammalian SWI/SNF (BAF) complexes are multi-component machines that remodel chromatin architecture. Dissection of the subunit- and domain- specific contributions to complex activities is required to advance mechanistic understanding. Here we examine the molecular, structural, and genome-wide regulatory consequences of recurrent, single- residue mutations in the putative coiled-coil C-terminal domain (CTD) of the SMARCB1 (BAF47) subunit which cause the intellectual disability disorder, Coffin-Siris syndrome (CSS), and are recurrently found in cancers. We find that the SMARCB1 CTD contains a basic alpha-helix that binds directly to the nucleosome acidic patch and that all CSS-associated mutations disrupt this binding. Furthermore, these mutations abrogate mSWI/SNF nucleosome remodeling activity and enhancer DNA accessibility, without changes in genome-wide complex localization. Finally, heterozygous CSS-associated *SMARCB1* mutations result in dominant gene regulatory and morphologic changes during iPSC-neuronal differentiation. These studies unmask an evolutionarily conserved structural role of the SMARCB1 CTD that is perturbed in human disease.

Graphical Abstract
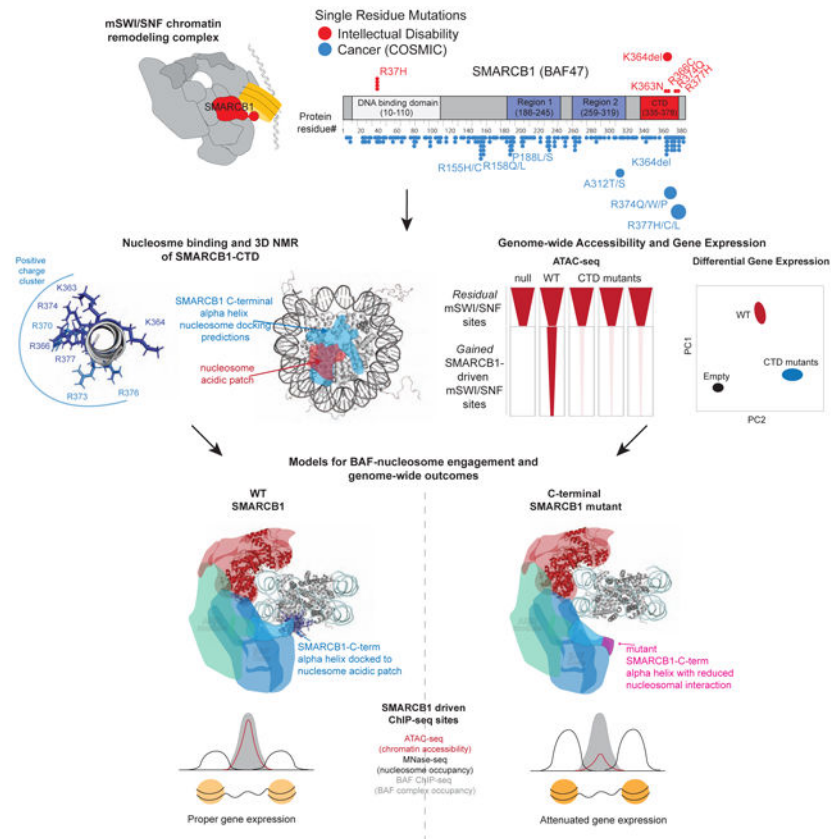
In brief

Genomic targeting and chromatin remodeling activities of SWI/Snf complexes are physically separable and can be selectively perturbed in disease contexts.

Introduction

Mammalian SWI/SNF (mSWI/SNF) ATP-dependent chromatin remodeling complexes are multisubunit, combinatorially assembled molecular machines that modulate chromatin architecture to enable DNA accessibility and gene expression (Clapier & Cairns 2009). mSWI/SNF complexes serve critical roles in cell division, cell and tissue differentiation, and development, and their perturbation is a frequent event in human disease, particularly in over 20% of human cancers (Kadoch et al. 2013; Kadoch & Crabtree 2015) and in specific neurodevelopmental disorders.

Exome sequencing efforts have recently identified autosomal dominant heterozygous mutations in mSWI/SNF subunit genes in individuals with intellectual disability (ID) syndromes and related cognitive disabilities (Ronan et al. 2013; Bögershausen & Wollnik 2018; Sokpor et al. 2017; Miyake et al. 2014; Santen et al. 2012; Santen et al. 2013; Santen et al. 2014; Tsurusaki et al. 2012; Tsurusaki et al. 2013; Wieczorek et al. 2013). However, the mechanisms by which these mutations alter mSWI/SNF complex structure and function on chromatin and subsequently lead to impaired cognitive and physical development remain unknown. Coffin-Siris Syndrome (CSS, OMIM # 135900) is a rare intellectual disability disorder in which over 60% of individuals harbor mutations in genes encoding members of the mSWI/SNF chromatin remodeling complex (Tsurusaki et al. 2013; Miyake et al. 2014; Kosho, Okamoto, et al. 2014). Individuals with CSS characteristically exhibit intellectual disability, coupled with a broad range of abnormalities spanning several organ systems, such as hypoplastic fifth digit nails, coarse facial features, generalized muscle hypotonia, immune system deficits, generalized hypertrichosis, sparse scalp hair, genitourinary and gastrointestinal complications, and congenital heart defects in >30% of individuals, at times requiring corrective heart surgery (Kosho, Okamoto, et al. 2014; Mannino et al. 2018; Santen et al. 2013; Kosho, Miyake, et al. 2014). CSS-associated heterozygous mutations occur de novo, that is, at the early stages of embryonic development. Given that the abnormalities observed in CSS individuals present across a range of organ systems indicates that the impact of CSS-linked mutations are not confined to a specific germ layer during development. While homozygous deletions of most mSWI/SNF genes are embryonic lethal in mice and hence would likely not result in live births, heterozygous mutations would be predicted to produce functional effects that are nuanced and/or partial, yet result in significant developmental consequences. Notably, de novo single amino acid mutations in the *SMARCB1* gene (which encodes the BAF47 or hSNF5 subunit; originally called INI1 (Kalpana et al. 1994)) accumulate within the highly conserved putative coiled-coil C-terminal domain (CTD) and are correlated with the most severe cases of intellectual disability implicated in CSS (Figure 1A, Figure S1A, Table S1). Enrichment of single residue mutations in the C-terminal domain of SMARCB1 are also found in cancers such as meningioma, adenocarcinoma, and schwannoma, among others (Tate et al. 2019; Forbes et al. 2011; Forbes et al., 2017; Schmitz et al., 2001). Biallelic inactivation of *SMARCB1* is the hallmark feature of malignant rhabdoid tumor and atypical teratoid/rhabdoid tumor, rare and highly aggressive pediatric cancers (Versteege et al. 1998). While SMARCB1 is one of the most evolutionarily conserved SWI/SNF subunits and has been studied in yeast, fly, and mammalian contexts for decades (Cairns et al., 1994; Dechassa et al., 2008; Dutta et al.,

2017; Kwon and Wagner, 2007; Peterson et al., 1998; Phelan et al., 1999; Sen et al., 2017; Versteege et al., 1998; Wang et al., 1996; Workman and Kingston, 1998), the specific role for its C-terminal domain and hence the impact of such mutations on mSWI/SNF complex function is unknown.

While high-resolution 3D structures of mSWI/SNF complexes have not to date been achieved, owing in large part to heterogenous composition and challenges in recombinant complex or subcomplex reconstitution, several recent studies have provided new insights of relevance to structure-function linkage. One such study is a detailed characterization of the modular organization and order of assembly of mSWI/SNF family complexes (Mashtalir et al. 2018), which used physical cross-linking mass spectrometry coupled with genetic deletions to assign subunit-subunit interfaces, the impact of disease-associated mutations on subunit assembly and stability, and the modular architecture of complexes in solution. Further, cryo-EM-determined binding of the yeast SNF2 helicase subunit to the nucleosome (Liu et al. 2017), and characterization of related chromatin remodeler family ATPase subunit interactions with the nucleosome acidic patch (Dann et al. 2017) have begun to define the mechanisms and determinants of remodeling activity, respectively, at least for the ATPase (catalytic) subunits. However, it remains to be determined if and where other subunits of mSWI/SNF complexes interact directly with nucleosomes and how these interactions impact overall complex function.

Here we used biochemical, structural, genomic, and cell differentiation approaches to demonstrate that the SMARCB1 CTD directly binds to the nucleosome acidic patch to enable mSWI/SNF complex-mediated nucleosome remodeling activity in vitro and genome-wide chromatin accessibility in cells. Specifically, using NMR, photocrosslinking, and molecular docking-based structural approaches, we determined that the SMARCB1 C-terminal alpha helical domain contains a dense region of basic, positively-charged amino acids, which directly bind the acidic patch region of the nucleosome. We find that single amino acid mutations within this region, which cause the intellectual disability syndrome CSS and are also frequent in cancer, or mutations which disrupt the integrity of the nucleosome acidic patch, hinder SMARCB1: nucleosome binding and mSWI/SNF complex remodeling. These findings decouple the genome-wide binding (localization on chromatin) of mutant mSWI/SNF complexes from their nucleosome remodeling activity and reveal the underlying mechanism by which mutations in the SMARCB1 c-terminal domain exert a dominant negative effect on mSWI/SNF activities in both CSS and cancer.

Results

Coffin-Siris syndrome-associated mutations occur across several mSWI/SNF subunit genes, largely those we have previously characterized to encode subunits within a 'core functional module' (Pan et al. 2018) and in genes specific for the canonical BAF (cBAF) subcomplex within the mSWI/SNF complex family (Pan et al. 2018; Mashtalir et al. 2018; Michel et al. 2018) (Figure S1B-C). The most recurrent CSS-associated mutation is an in-frame deletion of a single lysine, K364del (identified in 9 independent CSS cases), in the C-terminal putative coiled-coil domain of SMARCB1, situated near a variety of missense mutations, including R377H, K363N, R366C, and R374Q (4 cases in independent families) also in this

region (Figure 1A). Notably, single amino-acid mutations within the C-terminal region of SMARCB1 also occur in cancers (Figure 1, Figure S1A, Table S1; COSMIC database).

To biochemically evaluate the effects of these mutations on mSWI/SNF protein complex assembly and integrity, we first introduced SMARCB1 wild-type (WT) and mutant variants into SMARCB1-knockout HEK-293T cells (Figure S1D-E). WT and CSS-associated mutant SMARCB1 variants were stable at the total nuclear protein levels and stably incorporated into mSWI/SNF complexes irrespective of SMARCB1 mutation status, as indicated by immunoprecipitation studies followed by immunoblot, proteomic mass spectrometry and silver staining (Figure 1B-D, Figure S1F-G, Table S2). These data are consistent with the fact that we identified tandem repeat domains within the SNF5 homology region (RPT1 and RPT2) as essential for SMARCB1-mSWI/SNF complex binding (Figure S1H), and indicate that CSS-associated single residue mutations in the SMARCB1 CTD do not affect BAF complex integrity or assembly, pointing toward alternative functional consequences.

To assess possible changes in mSWI/SNF complex function, we subjected purified endogenous, fully-formed mSWI/SNF complexes containing either WT SMARCB1 or CSS-associated SMARCB1 variants, as well as a Kleefstra syndrome-associated SMARCB1 mutant variant containing the R37H mutation in the Winged-helix (WH) DNA binding domain (Diets et al. 2018; Kleefstra et al. 2012) (Figure 1D) to DpnII-mediated 601 mononucleosome restriction enzyme accessibility assays (REAA) to evaluate nucleosome remodeling activity (Figure 1E). Intriguingly, we found that complexes containing CSS-associated SMARCB1 CTD mutant variants exhibited significant attenuation in nucleosome remodeling activity compared to those containing WT SMARCB1 or R37H DNA-binding domain mutant SMARCB1 (Figure 1F-G, Figure S1I-J). In addition, we found a significant reduction in ATPase activity of SMARCB1 CTD mutant mSWI/SNF complexes relative to WT complexes when bound to nucleosome substrates (recombinant tetrameric polynucleosomes, and HeLa cell polynucleosomes), but no differences were detected when in solution with free 601 Widom DNA without the histone octamer, suggesting decreased mSWI/SNF remodeling activity and ATP consumption in the context of a complete nucleosome substrate (Figure 1H-J, Figure S1K-L). Taken together, these data unmask a specific compromise to the hallmark function of mSWI/SNF chromatin remodeling complexes rendered by single residue CSS-associated SMARCB1 CTD mutations (but not by mutations in the N-terminal DNA-binding domain).

Given these results, we next sought to determine whether the remodeling defect observed upon mutation of the SMARCB1-CTD could be due to altered interactions between mSWI/SNF complexes and their nucleosome substrates. Of note, while nucleosomes are well-established to be the key substrates of mSWI/SNF complexes, the specific interaction surfaces among the ~11-15 mSWI/SNF subunits with nucleosomes remains unknown with the exception of the recently-characterized yeast Snf2 helicase domain solved with nucleosomal DNA (Liu et al. 2017). To this end, we generated biotinylated peptides corresponding to amino acids 351-385 of SMARCB1 (minimal putative coiled-coil domain and the most highly conserved region within the c-terminal domain of SMARCB1), in either WT or CSS-associated mutant forms (Figure 2A, Figure S2A). Strikingly, we found that this 35-aa minimal region of the WT SMARCB1 c-terminal domain was sufficient to bind

mammalian mononucleosomes (Figure 2B, Figure S2B) and that all CSS-associated CTD mutations completely disrupted this binding interaction (Figure 2B). Importantly, incubation of CTD peptides with DNA did not produce changes in gelshift assays (EMSA) relative to WH DNA-binding domain protein, further confirming this as a protein-protein interaction with the histone octamer of the nucleosome rather than a protein-DNA interaction (Figure S2C).

Considering that SMARCB1 is one of the most conserved members of the SWI/SNF family, with high degrees of conservation back to yeast SNF5 (Figure S2D) and has been shown to play important roles in ATP-dependent chromatin remodeling in yeast SWI/SNF (Sen et al. 2017; Dutta et al. 2017) and other systems (Phelan et al. 1999; Nakayama et al. 2017; Wang et al. 2017), we sought to determine whether the minimal 35 aa C-terminal domains across species similarly bound nucleosomes. Indeed, all SNF5-like minimal CTDs exhibited clear binding to mononucleosomes, indicating conservation of this critical interaction throughout evolution (Figure 2C). Additional point mutations within the *H. sapiens* SMARCB1 CTD, including changes of lysine 364 to glutamine, alanine, proline residues, but not to a similarly charged arginine residue, also resulted in attenuated or completely abrogated SMARCB1 CTD-nucleosome binding (Figure S2E).

To characterize the effect of these mutations on SMARCB1 CTD secondary structure, we first used circular dichroism (CD) spectroscopy. This revealed that the CTD domain is alpha-helical in nature and that CSS-associated mutations do not grossly disrupt this secondary structure (Figure S2F). We next recombinantly expressed SMARCB1 CTD protein (aa 351-385) in heavy-labeled media (^{13}C, ^{15}N) for structural determination by nuclear magnetic resonance (NMR) spectroscopy (Figure S2G). T2 relaxation and secondary structure prediction of ^{15}N labeled SMARCB1-CTD provided evidence that the SMARCB1 C-terminal domain contains an alpha-helix (aa 357-377) flanked by residues that appear to be in highly dynamic random coil state (Figure S2H). Chemical shift assignments and backbone resonances were obtained using a set of seven triple-resonance experiments (the assigned ^{15}N-HSQC fingerprint spectrum is shown in Figure 2D). Ultimately, fifty structural models with 422 NOE distance restraints and 15 identified hydrogen-bonds were calculated using the XPLOR-NIH (Schwieters et al., 2003). A high-resolution structure of the alpha helical region of the SMARCB1-C terminus (aa 358-377) was obtained (0.15 −/+ 0.04 Å backbone root mean squared deviation for the top 10 determined structures) (Figure 2E; Table S3). Strikingly, the structures reveal an outward-facing positive charge (basic, K (Lys), R (Arg)) cluster of amino acids (Figure 2F, Figure S2I), several of which are those specifically mutated in CSS (Figure 1A). Analysis of the alpha helical structure (barrel view) further identified a dense cluster of 6+, highly conserved basic residues (Figure 2F, S2J). Moreover, electrostatic calculations using ABPS indicate that this arrangement leads to a positive charge cluster in the domain with the highest electrostatic potential calculation relative to the remainder of this region (Figure 2G), with all CSS-associated mutations predicted to significantly alter the isoelectric point (pI), net charge, or charge orientation of this region (Figure S2K-N). While the K364del mutation disrupts the ordered register of the helix, hence repositioning acidic residues within the CTD alpha helix onto the same face as the basic charge cluster, the missense mutations decrease the charge potential and abrogate association to the acidic nucleosome residues. These data collectively highlight distinct

mechanisms of structural disruption to the SMARCB1 C-terminal alpha helix, which uniformly perturb a critical mSWI/SNF: nucleosome interface.

To determine the region of the nucleosome to which the SMARCB1 CTD interacts, we adopted a photocrosslinking strategy in which a reactive diazirine probe was incorporated at various locations on the nucleosome surface [Dao et al., manuscript submitted; see STAR methods for details] (Figure 3A). This 'photoscanning' approach indicated that the SMARCB1 CTD interacts with an extended region of the nucleosome that includes the canonical acidic patch, a key binding epitope on the nucleosome surface (Dann et al. 2017) (interaction sites H2AE91 and H4E52, and to a lesser extent H2AE64, H2BE113) (Figure 3B-C). Notably, both K364del and R377H mutations led to a reduction in crosslinking across experiments (Figure 3B-D). In agreement with the crosslinking results, we found that mutations known to disrupt the integrity of the acidic patch significantly reduced binding of the SMARCB1 CTD (Figure 3E). Interestingly, the interaction was only partially antagonized in competition experiments employing LANA peptide, which is known to engage the canonical acidic patch region (Figure S3A-C), consistent with the idea that the SMARCB1 CTD interacts with a nucleosome surface epitope that extends beyond the canonical acidic patch region bound by LANA, which was further computationally predicted using ZDOCK (Figure 3F, Figure S3D-H). Taken together, these studies establish that the SMARCB1 CTD (aa 351-385) binds the nucleosome acidic patch, explaining the critical role for this minimal region in endogenous mSWI/SNF complex-mediated nucleosome remodeling, and the consequent impact of its disruption in intellectual disability syndromes and cancer (Figure 1).

To assess these functions in the context of human cell lines and at a genome-wide level, we leveraged the *SMARCB1*-deficient TTC1240 and G401 malignant rhabdoid tumor (MRT) cell lines and performed rescue experiments with either WT SMARCB1 or a series of CSS-associated SMARCB1 mutants, including deletion of the entire CTD (Figure 4A, Figure S4A). Treatment of these cells with the protein synthesis inhibitor, cycloheximide (CHX) demonstrated that FL and mutant SMARCB1 variants were stable across the 6-hour time course in TTC1240 (Figure S4B), in agreement with biochemical findings indicating complex integrity and abundance are not compromised with SMARCB1 mutants (Figure 1B-D). Previously, we and others identified that rescue of MRT cell lines with WT SMARCB1 resulted in genome-wide increases in mSWI/SNF complex occupancy, particularly at TSS-distal enhancer sites, and that restoration of complex occupancy over these sites correlated with an increase in enhancer activation as assessed by presence of the H3K27 acetylation mark (Nakayama et al., Nat. Gen. 2017, Wang et al., Nat. Gen. 2017). Surprisingly, in comparing the genome-wide targeting of BAF complexes in SMARCB1 WT and CSS-associated mutant conditions we found that WT and mutant variants exhibited nearly identical genome-wide targeting (Figure 4B, Figure S4C-D). Moreover, expression of both WT and mutant SMARCB1 variants resulted in similar increases in H3K27ac occupancy over gained SMARCB1/SMARCC1-bound distal sites, suggestive of enhancer activation (Figure 4B). However, when we examined DNA accessibility over these gained BAF complex sites using ATAC-seq, we found that CSS-associated SMARCB1 mutants generated substantially diminished accessibility relative to WT SMARCB1 (Figure 4C-D). This was also true at residual, promoter-proximal sites (sites to which BAF complexes were

targeted irrespective of SMARCB1 status) (Figure 4D). To assess more directly whether the diminished DNA accessibility correlated with reduced nucleosome occupancy, we performed MNase-seq in the empty vector control, WT SMARCB1, and K364del mutant conditions. MNase-seq fragment length distribution analysis confirmed the majority of reads were of mononucleosomal length (Figure S4E). Mapping MNase-seq reads over CTCF sites demonstrated no differences in nucleosome phasing between Empty, WT, or K364del mutant conditions, as recently demonstrated in mouse ES cells in the presence or absence of Smarca4 (Brg1) (Barisic et al., 2019) (Figure S4F). Interestingly, however, MNase-seq metaplot analysis at the SMARCA4 ChIP-seq peaks showed decreased nucleosome occupancy (greater nucleosome eviction) for the WT compared to K36del mutant or Empty conditions (Figure 4E). Furthermore, in line with ATAC-seq results, we found that the K364del exhibited reduced nucleosome eviction at the gained BAF complex sites, as indicated by a depletion of MNase-seq signal at the center of the SMARCA4-gained peaks (Figure 4E). These results are exemplified at the *RFTN1* and *CAPZB* loci (Figure 4F, Figure S4G-I) and differences between conditions are captured by principle component analysis (PCA) of ATAC-seq signals over SMARCB1 peaks (Figure 4G). Comparing differential accessibility between SMARCB1 variant conditions revealed that the majority of significantly changed sites exhibited decreases in accessibility in the mutant SMARCB1 conditions relative to WT (Figure S4J). Finally, we observed that these changes in chromatin accessibility were manifested globally at the mRNA level (Figure S4K), with PCA of corresponding RNA-seq showing marked separation between empty vector, SMARCB1 WT, and CSS-associated CTD mutant conditions (Figure 4H). These results were recapitulated in the G401 SMARCB1-deficient MRT cell line (Figure S4L-M). Finally, clustering of ATAC-seq and RNA-seq datasets revealed a subset of ATAC-seq sites gained in the WT SMARCB1 rescue setting that showed decreased gene expression in the mutant conditions relative to WT in both TTC1240 and G401 cell lines (Figure S4N). Metascape analysis of these sites revealed a number of developmental processes such as vasculature development, heart development, skeletal system development, regulation of neurogenesis, among others (Figure S4O).

Taken together, these results establish a role for the SMARCB1 CTD in mediating mSWI/SNF-driven DNA accessibility rather than genome-wide complex targeting. These genome-wide findings closely align with results of in vitro ATPase activity and nucleosome remodeling assays performed in vitro with endogenously-purified complexes (Figure 1), pointing to a specific mechanism that is coopted via mutations in the CTD of SMARCB1 in CSS, a neurodevelopmental condition that has enabled the uncoupling of mSWI/SNF remodeling activity and targeting on chromatin. Mutations in the SMARCB1 CTD stand in stark contrast to mutations or deletion of the winged-helix DNA binding domain (N-terminus) that we found do not disrupt mSWI/SNF-mediated nucleosome remodeling in vitro (Figure 1G-J), or alter DNA accessibility in cells (Figure S4P), furthering the concept that mSWI/SNF activities can be disrupted at distinct functional axes.

Finally, to assess the phenotypic consequences of SMARCB1 C-terminal domain mutations in a heterozygous setting (mimicking the gene status of individuals with CSS), we generated human induced pluripotent stem cells (iPSCs) genetically modified to harbor heterozygous *SMARCB1* c-terminal mutations, particularly K364del (Figure 5A) which we could then

differentiate toward neuronal lineage using a neurogenin (Ngn2)-based neuronal differentiation protocol (Yingsha Zhang et al. 2013). Briefly, heterozygous SMARCB1 mutant SAH iPSCs were generated using homology directed repair (HDR) with a mutant single-stranded oligodeoxynucleotide (ssODN) donor template introduced with CRISPR-Cas9 reagents targeting the *SMARCB1* gene 3'-end (Figure S5A). Mutations were confirmed by sequencing of the *SMARCB1* gene (Figure S5B). Baseline WT and mutant iPSCs exhibited similar cell health profiles as assessed by flow cytometry-based analysis of early (Annexin-V (V CF Blue)), and late (7-AAD) stage apoptosis markers (Figure S5C). In undifferentiated SAH iPSCs, genome-wide BAF complex targeting as well as H3K27ac occupancy was comparable between WT and the SMARCB1 K364del mutant settings, however, nearly 25% of sites exhibited statistically significant decreases in DNA accessibility in the K364del mutant relative to WT, as measured by ATAC-seq (Figure 5B). Interestingly, while all analyzed ChIP-seq signals were comparable or increased in the K364del/+ versus WT condition over merged SMARCA4 peaks, ATAC-seq signal decreased (Figure 5C, Figure S5D). HOMER and LOLA motif analysis of sites with reduced DNA accessibility in the K364del mutant condition were enriched for OCT, SOX, and NANOG motifs, suggesting decreased accessibility at pluripotent factor gene loci, as exemplified also at the *ANKRD1* locus (Figure 5D, Figure S5E-F). At baseline, differential gene expression analysis and GSEA studies performed on Day 0 (undifferentiated) iPSCs comparing wild-type versus K364del iPSCs indicated a range of processes affected in beyond nervous system processes, including cardiac muscle development, kidney and mesenchyme development, endocrine system development, and cell fate commitment, in agreement with physiologic findings in CSS individuals (Fig. S5G-H). In order to visualize transcriptional changes between the SMARCB1 WT and K364del conditions during differentiation, expression levels of differentially expressed genes derived from days 0, 2, 4, and 8 were partitioned into 6 groups by k-means clustering and displayed in heatmap form (Figure S5I). A substantial divergence in transcription was observed at day 8, as shown in clusters 5 and 6. Intriguingly, cluster 6 genes, which appeared less activated in the mutant condition, were enriched for developmental processes (Figure 5E, Figure S5J) and overlapped with nearly 100 genes (n=91) that are mutated in intellectual disability syndromes (Vissers et al. 2016) and those normally upregulated during Ngn-2 induced differentiation (Yingsha Zhang et al. 2013) (n=749 total) suggesting a convergence between the consequences of individual mutations of these genes and the effect of mSWI/SNF master regulatory complex perturbations (Figure 5F, Table S4). Through a similar approach examining ATAC-seq on Day 4 versus 0 of the Ngn2-differentiation protocol, we observed increases in DNA accessibility at a number of enhancers (C1 and C2) in the WT condition, which did not increase in the K36del mutant condition (C1) (Figure S5K-L). Metascape analysis performed on clusters C1 and C2 showed that both clusters enriched for neurodevelopmental processes, suggesting that the mutant condition was unable to appropriately open and thereby activate appropriate neurodevelopmental processes (Figure S5M). Indeed, ID-associated genes such as *ASCL1, FGFR2, GLI3, PAX6, SOX10* and others exhibited significant blocks in activation during the neurogenin-induced differentiation time course in SMARCB1 K364del mutant iPSCs (Figure 5G).

Last, we explored the morphologic properties of differentiated neurons derived from WT SMARCB1 versus SMARCB1 K364del and heterozygous KO (indel) mutant iPSCs. We found significantly diminished neurite outgrowth (length) and neuron counts (at days 6, 8 and 10) in SMARCB1 CSS mutant cells (either K364del or indel) relative to WT control cells (Figure 5H-I, Figure S5N-O), recapitulating differentiation deficits observed in patient-derived models of developmental delay (Sheridan et al., 2011) and recent studies examining related heterozygous Nicolaides-Baraitser Syndrome associated mutations of the *SMARCA2* gene (Gao et al., 2019). Notably, rescue of WT SMARCB1 in heterozygous K364 and indel iPSCs resulted in substantial rescue of both neuron counts and neurite outgrowth (Figure 5H-J, Figure S5N). Further, we used NGN2 (FITC) fluorescence imaging to confirm NGN2 (neuronal differentiation marker) expression as well as microtubule-associated TUJ1 (neuron-specific class III beta tubulin) immunofluorescence staining to visualize neuronal projections. Through this, we found that K364del and heterozygous KO cells developed significantly fewer neuronal projections compared to WT control cells upon neurogenin differentiation, phenotypes which were rescued by restoration of WT SMARCB1 (Figure 5J, Figure S5O). These data highlight the role for mSWI/SNF-mediated chromatin remodeling facilitated by the SMARCB1 C-terminal domain during neuronal differentiation and provide a mechanistic rationalization for the neurodevelopmental features of CSS.

Discussion

Here we have identified a critical structural and functional role for the SMARCB1 CTD in nucleosome remodeling and enhancer DNA accessibility by interrogating point mutations found in individuals with the intellectual disability, Coffin-Siris Syndrome. Our in vitro and cell-based studies demonstrate that CSS-associated SMARCB1 mutations result in compromised (though, importantly, not absent) mSWI/SNF functional activity. Unexpectedly, we find that mSWI/SNF complexes containing single-residue mutations in the SMARCB1 C-terminal alpha helical domain exhibit similar targeting on chromatin genome-wide, but are defective in generating DNA accessibility and in activating critical target genes, marking a first time in this field in which we have observed that mSWI/SNF targeting and DNA accessibility do not mirror one another. For example, these data present an interesting contrast to recent studies examining ATPase-active versus -inactive BAF complexes, in that complexes lacking ATPase catalytic activity (via point mutations in the ATPase/helicase domain of SMARCA4/SMARCA2) are both unable to target to and open and activate distal sites (Pan et al., 2019). Here we show that CSS-associated SMARCB1 mutations result in a retained ability of mSWI/SNF complexes to target to distal enhancer sites (and to recruit H3K27ac), but an inability to create DNA accessibility to the levels of wild-type complexes. These complementary investigations provide an opportunity to uncouple the roles of proper nucleosome remodeling and mSWI/SNF complex localization, as well as recruitment of other complexes (i.e. P300) to place activating histone marks (i.e. H3K27Ac) at differentially poised chromatin landscapes. These results further highlight a fundamental difference between focused point mutations in the CTD domain and complete loss of the SMARCB1 subunit (biallelic deletion) in MRT (Nakayama et al. 2017), again which shows complete loss of targeting to distal enhancer sites genome-wide.

Of note, we found that SMARCB1 C-terminal mutant mSWI/SNF complexes, which exhibited decreased remodeling activity and decreased ATP consumption on nucleosome substrates in vitro, trended toward increased chromatin occupancy compared to complexes with WT SMARCB1, suggesting longer residence times and potential "stalling" of mSWI/SNF movement (Figure 4F, S4G). This was further complemented by MNase-seq studies which indicated genome-wide increased occupancy of flanking nucleosomes on either side of the BAF complex peaks in the CSS-associated mutant versus SMARCB1 WT conditions.

Apart from the recently described yeast Snf2 helicase domain: nucleosome DNA double helix structures (Liu et al., 2017), interactions between mSWI/SNF subunits and the nucleosome and their impacts on overall complex function have not been described. Here, by focusing on the SMARCB1 C-terminal domain owing to frequent mutations in ID and cancer, we identify a dense cluster of basic, positively charged amino acids within an alpha-helical structure that are required for SMARCB1 nucleosome acidic patch binding, and hence the mSWI/SNF complex core module: nucleosome acidic patch engagement (Mashtalir et al., 2018). Marrying these data with those of Cheng and colleagues (Li et al, 2017) and Mashtalir and colleagues, and using H2AE91 restraint-containing simulations, we propose a model for mSWI/SNF complex: nucleosome engagement (Figure 6A), and highlight how CSS-associated point mutations in the CTD domain inhibit mSWI/SNF complex: nucleosome binding. We suggest that inhibition of remodeling of mSWI/SNF complexes on their nucleosomal substrates then results in reduced DNA accessibility, reduced nucleosome displacement (and hence increased nucleosome occupancy) at BAF target sites, and reduced gene expression (Figure 6B, C).

There is significant interest by the global research community in developing small molecule inhibitors of mSWI/SNF complex activities. While the majority of drug discovery efforts have been directed toward ATPase inhibition (i.e. catalytic inhibition of the SMARCA4 and SMARCA2 components), the SMARCB1 CTD: nucleosome interface described here is the first allosteric interface identified that, if disrupted via small molecules, would be expected to specifically inhibit the remodeling activity of mSWI/SNF complexes, and even of specific subcomplexes within the mSWI/SNF family (canonical BAF and PBAF, but not ncBAF as ncBAF does not contain the SMARCB1 subunit). Our findings suggest exciting future work to chemically inhibit or attenuate mSWI/SNF remodeling activities.

Finally, at the transcriptional and cell physiologic levels, our results highlight and reinforce the importance of mSWI/SNF-mediated chromatin remodeling for the maintenance of stem cell pluripotency factors and their networks (Singhal et al. 2010), as well as for cell type-specific development, such as nervous system differentiation, explored here. We emphasize that CSS individuals provide evidence that heterozygous mutations across a variety of mSWI/SNF genes allow for viability, in contrast to homozygous missense mutations which we hypothesize would be embryonically lethal. Nevertheless, it is important to highlight the limitations of such a model, including (1) variability of single-cell clones post CRISPR-mediated editing; (2) the fact that these iPSCs do not model three dimensional tissue cultures such as cerebral organoids or animal model systems; and (3) by generating the mutations in iPSCs (despite the fact that this is not definitively the state at which the

mutation is acquired in human development), transcriptional changes are already detected at this stage, followed by different changes occurring during, in this case, neurogenin-based differentiation.

With human genetics, biochemistry, structural biology woven together, this study highlights the power of examining recurrent disease-associated mutations to advance our mechanistic understanding of mSWI/SNF complex function in healthy and disease states.

STAR Methods Text

LEAD CONTACT AND MATERIALS AVAILABILITY

Further information and requests for resources and reagents should be directed to and will be fulfilled by the Lead Contact, Cigall Kadoch (Cigall_kadoch@dfci.harvard.edu). All unique/ stable reagents generated in this study are available from the Lead Contact with a completed Material Transfer Agreements.

EXPERIMENTAL MODEL AND SUBJECT DETAILS

Mammalian cell lines and culture conditions—The TTC1240 (female), G401 (male), and 293T (female) SMARCB1 knockout ($293T^{SMARCB1\,-/-}$) cells were cultured in standard DMEM (Gibco), supplemented with 10% FBS (Omega), 1X GlutaMAX (Gibco), 100 U/mL penicillin-streptomycin (Gibco), 1mM sodium pyruvate (Gibco), 1X MEM NEAA (Gibco), 10 mM HePES (Gibco), 1X 2-mercaptoethanol (Gibco) and maintained in a humidified incubator at 37°C with 5% CO_2.

The SAH (SAH0047-02; female) induced-pluripotent stem cell (iPSC) line was generated in Dr. M. Sahin's laboratory at Boston Children's Hospital (Ebrahimi-Fakhari et al., 2016) and a generous gift from Dr. Clifford Woolf's laboratory at Boston Children's Hospital. The wild-type and mutant SAH iPSCs were maintained in StemFlex Medium (Gibco) prior to differentiation.

Bacterial strains used for protein production—*Escherichia coli* BL21(DE3) and Rosetta (DE3) cells were used for the expression of the SMARCB1-CTD (aa351-385) and SMARCB1-WH DNA Binding domains, respectively. Growth and protein expression conditions are outlined in the method details.

METHOD DETAILS

***SMARCB1* CRISPR-Cas9 genome editing**—The $293T^{SMARCB1\,-/-}$ cell line was generated using the *Ini1* CRISPR/Cas9 KO and *Ini1* HDR plasmids (Santa Cruz Biotechnology, sc-423027; sc-423027-HDR) following the manufacturer's protocol as previously described in (Nakayama et al. 2017).

The SAH iPSC line underwent CRISPR/Cas9 mediated genome editing with a short-guide RNA (sgRNA, 5'-GGAGAAGAAGATCCGCGACC **AGG**-3') targeting exon 8 of the SMARCB1 gene and a single-stranded oligodeoxynucleotide (ssoDn, 5'- CCGGAACACG GGCGATGCGG ACCAGTGGTG CCCACTGCTG GAGACTCTGA CAGACGCTGA GATGGAA-A--A**A**AT**A**CGCG A**T**CA**A**GACAG GAACACGAGG TACCCCTGGC

CCTGTGGTCC TGGGCTCTGC CCACAGGCAC CTGGCTTTCC -3'; silent mutations emphasized in red) donor strand encoding for the SMARCB1 K364del in-frame deletion. Specifically, cells were nucleofected with a ssODN donor and CRISPR/Cas9 plasmid (px458) that was constructed with hSMARCB1 distinct sgRNA using Amaxa 4D-Nucleofector. Fourty-eight hours after nucleofection, cells were single cell sorted by FACS, genotyped by PcR and then confirmed via standard TA-cloning procedures to obtain a *SMARCB1*+/+ wild-type control, a *SMARCB1*^K364del/+ heterozygous mutant, and a *SMARCB1* exon 8 indel mutant (*SMARCB1*^p.(I349Lfs*)/+).

Nuclear extract—Nuclear extracts for TTC1240 and 293T *SMARCB1* knockout cells were prepared as described in (Mashtalir et al. 2018). Specifically, cells were scraped from plates, washed with cold PBS, pelleted at 1,200 rpm for 5 min at 4°C, and resuspended in EB0 hypotonic buffer (50 mM Tris, pH 7.5, 0.1% NP-40, 1 mM EDTA, 1 mM $MgCl_2$ supplemented with protease inhibitor (Roche), and 1 mM phenylmethylsulfonyl fluoride (PMSF)). Lysates were pelleted at 5,000 rpm for 5 min at 4°C. Supernatants were discarded, and nuclei were resuspended in EB300 high salt buffer (50 mM Tris, pH 7.5, 300 mM NaCl, 1% NP-40, 1 mM EDTA, 1 mM $MgCl_2$ supplemented with protease inhibitor and 1 mM PMSF). Lysates were incubated on ice for 10 min with occasional vortexing. Lysates were then pelleted at 21,000 x g for 10 min at 4°C. Supernatants were collected, and protein concentrations were quantified via bicinchonic acid (BCA) assay (Pierce). Finally, samples were supplemented with 1 mM DTT.

Co-immunoprecipitation—For immunoprecipitation of 293T$^{SMARCB1 \; / \;}$ nuclear extracts, 700 μg of nuclear extract (at 1 μg/μL) were incubated with 2-5 μg of antibody (Table S2) overnight at 4°C. Dynabeads (Pierce Protein G Magnetic Beads, Thermo Scientific) were then added, rotated for 2 hours at 4°C, and washed 3-5 times with EB300. Beads were eluted with sample buffer (2X NuPAGE LDS Buffer (Invitrogen) and 200 mM DTT) to load onto an SDS-PAGE gel.

For immunoprecipitation of G401 nuclear extracts, 200 μg of nuclear extract were incubated with 2 μg of antibody in IP Buffer rotating overnight at 4°C. Samples were then incubated with Dynabeads (Pierce Protein G Magnetic Beads, Thermo Scientific) rotating for 2 hours at 4°C. Beads were washed 3 times in IP Buffer, once with BC100 (20 mM HEPES, 100 mM KCl, 0.2 mM EDTA, 10% glycerol), and eluted with 20 μL of sample buffer (1X NuPAGE LDS Buffer (Invitrogen) and 100 mM DTT) to load onto an SDS PAGE gel.

Western Blotting—Western blot analysis was performed using standard procedures. For western blots visualizing mSWI/SNF complex subunits, samples were separated using a 4-12% Bis-Tris PAGE gel (NuPAGE 4-12% Bis-Tris Protein Gel, Invitrogen), and transferred onto a PVDF membrane (Immobilon-FL, EMD Millipore). For western blots visualizing histones, samples were separated using a 10-20% tricine gel (Novex 10-20% Tricine Protein Gel, Themo Scientific), and transferred onto a PVDF membrane (Immobilon-PSQ, EMD Millipore). Membranes were blocked with 5% milk in PBST and incubated with primary antibody (Table S2) for 3 hours at RT or overnight at 4°C. Membranes were washed 3 times with PBST and then incubated with near-infrared fluorophore-conjugated species-specific secondary antibodies (LI-COR) for 1 hour at RT.

Following secondary, membranes were washed 3 times with PBST, once with PBS, and then imaged using a Li-Cor Odyssey CLx imaging system (LI-COR).

Purification of mSWI/SNF complexes—mSW/SNF complex purification was performed essentially as described in (Mashtalir et al. 2018). Briefly, stable 293T$^{SMARCB1 ∕}$ cell lines infected with HA-tagged SMARCB1 variants or full-length SMARCE1 were expanded to obtain necessary bait expression levels. Cells were scraped from plates, washed with cold PBS, and centrifuged at 5,000 rpm for 5 min at 4°C. Pellets were resuspended in hypotonic buffer (HB: 10 mM Tris HCl, pH 7.5, 10 mM KCl, 1.5 mM MgCl$_2$, supplemented with 1 mM DTT and 1 mM PMSF) and incubated for 5 min on ice. The suspension was centrifuged at 5,000 rpm for 5 min at 4°C, and pellets were resuspended in 5 volumes of HB containing protease inhibitor cocktail. The suspension was then homogenized using a glass Dounce homogenizer (Kimble Kontes). Suspension was layered onto HB sucrose cushion containing 30% sucrose (w/v) and centrifuged at 5,000 rpm for 1 hour at 4°C. The nuclear pellets were resuspended in high salt buffer (HSB: 50 mM Tris HCl, pH 7.5, 300 mM KCl, 1 mM MgCl$_2$, 1 mM EDTA, 1% NP40 supplemented with 1 mM DTT, 1 mM PMSF, and protease inhibitor cocktail). Homogenate incubated on rotator for 1 hour at 4°C. The supernatant was then centrifuged at 20,000 rpm (30,000 x g) for 1 hour at 4°C using a SW32Ti rotor. The high salt nuclear extract supernatant was filtered through a 25 mm quartz filter (Advantec QR-200 Quartz Fiber Filter, Cole-Parmer) and incubated with Pierce Anti-HA Magnetic Beads (Thermo Fisher) overnight at 4°C. HA beads were was hed 6 times in HSB and eluted with HSB containing 1 mg/mL of HA peptide (GenScript) for 4 x 1.5 hours each. Eluted proteins were then subjected to dialysis (Slide-A-Lyzer MINI Dialysis Device, 10K MWCO, Thermo Scientific) using Dialysis Buffer (25 mM HEPES, pH 8.0, 0.1 mM EDTA, 100 mM KCl, 1 mM MgCl$_2$, 15% glycerol, and 1 mM DTT) overnight at 4°C, and final ly concentrated using Amicon Ultra centrifugal filters (30 kDa MWCO, EMD Millipore).

Silver Stain—SMARCB1-HA WT and mutant variant containing mSWI/SNF complexes were purified via HA-epitope dependent complex purification. Samples were run on a 4-12% Bis-Tris SDS PAGE gel, stained using the SilverQuest Silver Staining Kit (Invitrogen), and imaged using an Epson-Perfection V600 Photo scanner.

Restriction Enzyme Accessibility Assay (REAA) Nucleosome Remodeling Assay—SMARCA4 (BRG1) levels of the HA-purified mSWI/SNF complex purifications were normalized via BCA protein quantification and Silver Stain analyses. Purified mSWI/SNF complexes were diluted for final reaction concentration of 10 ng/μL in REAA buffer (20 mM HEPES, pH 8.0, 50 mM KCl, 5 mM MgCl$_2$) containing 0.1 mg/mL BSA, 1 μM DTT, 20 nM nucleosomes (EpiDyne Nucleosome Remodeling Assay Substrate ST601-GATC1, EpiCypher). The REAA mixture was incubated at 30 or 37°C for 10 min, and reaction was initiated using 1-2 mM ATP (Ultrapure ATP, Promega) and 0.005 U/μL DpnII Restriction Enzyme (New England Biolabs). The REAA reaction mixture was quenched with 20-24 mM EDTA and placed on ice. Proteinase K (Ambion) was added at (100 μg/mL)_for 30-60 min, followed by either AMPure bead DNA purification and D1000 HS DNA ScreenTape Analysis (Agilent) or mixing with GelPilot Loading Dye (QIAGEN) and

loading onto 8% TBE gel (Novex 8% TBE Gels, Thermo Fisher). TBE gels were stained with either SYBR-Safe (Invitrogen) or Syto-60 Red Fluorescent Nucleic Acid Stain (Invitrogen), followed by imaging with UV light on an Alpha Innotech AlphaImager 2200 and/or with 652 nm light excitation on a Li-Cor Odyssey CLx imaging system (LI-COR).

ATPase assay (ADP Glo Kinase Assay)—ATPase consumption assays were performed using the ADP-Glo Kinase Assay kit (Promega). The same conditions as the REAA nucleosome remodeling assay described above were used, excluding the DpnII restriction enzyme. Following incubation with desired substrates for 60-90 min at either 30°C., 1X volume of ADP-Glo Reagent was used to quench the reaction and incubated at RT for 40 min. 2X volume of the Kinase Detection Reagent was then added and incubated at RT for 1 hour. Luminescence readout was recorded. Substrates used for this assay were purified 601 NCP DNA, recombinant histone octamer (EpiCypher, Cat#16-0001), recombinant mononucleosome (EpiDyne Nucleosome Remodeling Assay Substrate ST601-GATC1, EpiCypher, Cat#16-4101), recombinant tetranucleosomes (Reaction Biology, Cat# HMT-15-369), and HeLa polynucleosomes (EpiCypher, Cat# 16-0003). HA-purified mSWI/SNF complexes were used at 10ng/μL and 200 μg of material was used for each ARID1A-IP nuclear extract using ARID1A antibody (Cell Signaling, Cat# 12354S). Details of the IP-based assay will be described elsewhere (St. Pierre et al., *manuscript in preparation*).

SNF5 homology protein conservation analysis across species—*ConSurf Conservation Analysis*: Canonical (aa 1-385) and coiled coil (aa 332-385) SMARCB1 (Uniprot ID: Q12824) sequences were run through ConSurf (Ashkenazy et al. 2016) conservation analysis using UNIREF90 and MAFFT running parameters. *Phylogenetic trees:* Phylogenetic trees were created using Geneious with built alignment options for building distance matrix (Alignment type: global alignment with free end gaps, Cost Matrix: Blosum62) and Tree Builder Options (Genetics Distance Model: Jukes-Cantor, and Tree Build Method: UPGMA). *Similarity*: Geneious pairwise/multiple alignment tool was used to determine identity and similarity between SMARCB1 and other SNF5 homology proteins and their respective domains.

Peptide pulldown experiments—N-terminal biotin-labeled SNF5 homology coiled-coil peptide variants (including SMARCB1 variants) were obtained from KE Biochem (Table S3). Lyophilized peptides were diluted to 10 mM in DMSO and subsequently diluted to 1 mM in EB150 (50 mM Tris, pH 7.5, 150 mM NaCl, 0.1% NP-40, 1 mM EDTA, 1 mM MgCl$_2$ supplemented with 1 mM DTT, and 1 mM PMSF). Biotin-labeled peptides were diluted to 10 μM in EB150 and bound to Streptavidin Dynabeads (Pierce Streptavidin Magnetic Beads, Thermo Scientific) overnight at 4°C. Beads were washed 3 times in EB150, and 1-1.6 μg of mononucleosomes were added. The suspension was rotated for 5-7 hours at 4°C. The beads were washed 3-5 tim es in EB150, and eluted in Sample Buffer (2X LDS with 200 mM DTT) to load onto 10-20% Tricine gels. Following electrophoresis and PVDF membrane transfer, membranes were subjected to Ponceau Staining for peptide detection and/or Western Blotting for detecting the presence of nucleosome components.

LANA peptide competition—The LANA peptide competition was set up in a similar manner as the peptide pull down experiments with the following exceptions: SMARCB1-CC (aa 351-385) biotin-labeled peptides at 10 μM in EB150 were bound to Streptavidin Dynabeads (Pierce Streptavidin Magnetic Beads, Thermo Scientific) in parallel to 1-1.6 μg of mononucleosoes incubated with LANA peptide (KE Biochem) at varying concentrations ranging from 0-30 μM overnight at 4°C. Beads were washed 3 times in EB150, and resuspended with the mononucleosome/LANA peptide solutions. The suspension was rotated for 3-5 hours at 4°C. The be ads were washed 3-5 times in EB150, and eluted in Sample Buffer (2X LDS with 200 mM DTT) to load onto 10-20% Tricine gels.

Ponceau Stain—Immediately following transfer onto PVDF membrane, membrane was rinsed in PBST and stained using Ponceau-S solution (Sigma-Aldrich) for 1 hour at RT. Membrane was washed 3 times in milliQ H_2O and imaged on an Epson-Perfection V600 Photo scanner.

Cycloheximide Chase experiments to assess protein stability—7 Days following lentiviral infection of TTC1240 cells with Empty vector or SMARCB1 WT or c-terminal mutant constructs as described above, cells were plated at 400K cells/well in 24 well. On Day 9, cycloheximide was added (10 μM) sequentially at 6, 3, 1, and 0 (negative control) hours prior to cell lysis with 100 μL of SdS Lysis Buffer (1.5% SDS, 25 mM Tris, pH 7.5). Whole cell lysates were sonicated and protein concentrations were quantified by BCA and prepared for western blot analysis as described above.

Mammalian mononucleosomes purification—Mammalian mononucleosomes were purified from HEK293T cells similar to as described in (Mashtalir et al. 2014). Cells were scraped from plates, washed with cold PBS, and centrifuged at 5,000 rpm for 5 min at 4°C. Pellets were resuspe nded in hypotonic buffer (EB0: 50 mM Tris HCl, pH 7.5, 1mM EDTA, 1mM $MgCl_2$, 0.1% NP40 supplemented with 1 mM DTT, 1 mM PMSF, and protease inhibitor cocktail and incubated for 5 min on ice. The suspension was centrifuged at 5,000 rpm for 5 min at 4°C, and pellets were resuspended in 5 volumes of EB420 (EB0: 50 mM Tris HCl, pH 7.5, 420mM NaCl, 1 mM $MgCl_2$, 0.1% NP40 with supplemented with 1 mM DTT and 1 mM PMSF containing protease inhibitor cocktail. Homogenate incubated on rotator for 1 hour at 4°C. The supernatant was then centrifuged at 20,000 rpm (30,000 x g) for 1 hour at 4°C using a SW32Ti rotor. Supernatant was then discarded and chromatin pellet was washed in MNase buffer (20 mM Tris-HCl pH 7.5, 100 mM KCl, 2 mM MgCl2, 1 mM CaCl2, 0.3 M sucrose, 0.1% NP-40, and protease inhibitor cocktail) 3 times. Following MNase treatment (3 U/mL for 30 min at room temperature, Sigma-Aldrich), the reaction was quenched with 5 mM of EGTA and 5 mM of EDTA. The samples were then centrifuged at 20,000 x g for 1 hour at 4'C to obtain the soluble chromatin fraction. Soluble chromatin fraction was loaded onto 10-30% glycerol gradient (Mashtalir et al. 2018) and fractions containing mononucleosomes were isolated and concentrated using centrifugal filter (Amicon, EMD Millipore).

Vectors Used—Constitutive expression of C-terminal HA-tagged SMARCB1 (BAF47) variants (i.e. full-length, R37H, K363N, K364del, R366C, or   CC (aa 1-325) or N-terminal

HA-tagged full-length SMARCE1 (BAF57) in the 293T$^{SMARCB1\ /}$ cell line was achieved using lentiviral infection of an EF1α-driven expression vector (modified pTight vector from Clontech, dual promoter EF-1a-MCS-PGK-Puro), selected with puromycin (2 μg/μL, Sigma-Aldrich).

Constitutive expression C-terminal V5-tagged SMARCB1 (BAF47) variants (i.e. full-length, K364del, R377H, CC (aa 1-325), N-term (aa 177-385), C-term (aa 1-176), RPT1 (deletion of aa 186-245), RPT2 (deletion of aa 259-319), RPT1-2 (deletion of aa 186-319) in MRT and iPS cell lines was achieved using lentiviral infection of an EF1α-driven expression vector (modified pTight vector from Clontech, dual promoter EF-1a-MCS-PGK-Blast), selected with blasticidin (10 μg/mL, Thermo Fisher).

Lentiviral generation.—Lentiviral particles were prepared using LentiX HEK293T packaging cells (Clontech) via polyethylenimine-mediated transfection (PEI, Polysciences Inc.) of gene delivery vector co-transfected with packaging vectors pspax2 and pMD2.G as previously described (Forbes et al. 2011). Supernatants were harvested 72 hours after transfection and centrifuged at 20,000 rpm for 2.5 hours at 4°C. Virus containing pellets were resuspended in PBS, pH 7.4 (Gibco) and placed on cells dropwise.

Infection and selection.—TTC1240 cells and were lentivirally infected with either Empty vector, or one of four c-terminal V5-tagged SMARCB1 variant constructs (full length, K364del, R377H, or CC construct) for 48h and then selected with blasticidin (10 μg/mL), split at 72h and continued with selection for 5 days. Cells were harvested for biochemical, ChIP-seq, RNA-seq, and ATAC-seq experiments 7 days post-infection. For TTC1240 cells lentivirally infected with the N-term (aa 177-385) or C-term (aa 1-176) constructs, cells were harvested for ATAC-seq 9 days post-infection.

The 293T$^{SMARCB1\ /}$ cells were made into stable lines via lentiviral infection of either c-terminal HA-tagged full length, R37H, K363N, K364del, R366C, or CC SMARCB1 constructs followed by puromycin selection (2 μg/mL). The SAH $SMARCB1^{+/+}$, $SMARCB1^{K364del/+}$, and $SMARCB1^{p.(I340Lfs*)/+}$ iPS cells were made into stable lines via lentiviral infection with either Empty vector or C-terminal V5-tagged full-length SMARCB1 followed by blasticidin selection (10 μg/mL).

Cortical neuron differentiation of iPSCs.—Ngn2-induced cortical neuron differentiation protocol was adapted and slightly modified from (Yingsha Zhang et al. 2013). On Day -2, SAH cells were split and plated at 2K/well in Geltrex coated 96w plates. On D(−1), cells were transduced with lentivirus expressing rtTA, Ngn2 conjugated with puromycin resistant gene and EGFP. To induce NGN2-mediated differentiation, 2μg/ml Doxycycline (Clontech) was added to the DMEM/F12/NEAA/N2 medium (Gibco) supplemented with 10ng/ml human BDNF, 10ng/ml NT-3 and 0.2 μg/ml mouse laminin on D0. Following 24h puromycin (1μg/ml, InvivoGen) selection on D1, mouse glia or glia conditioned medium was added to the culture, and the medium was switched to Neurobasal/B27 containing BDNF, NT-3, laminin and 2μM Arc-C (Sigma) on D2. Half of the media was changed every other day on D3-6. 2.5% FBS (Gibco) was added to the medium from D7 to support glia viability. During differentiation, images were acquired by

Arrayscan XTI (ThermoFisher) high content imaging system periodically. The differentiated NGN2 neurons were also fixed at DIV 6, 8 and 10 of differentiation and imaged for FITC (NGN2) and stained with DAPI and TUJ1 antibody for automatic quantification of total neuronal counts, average neuron length, and total cell count using ImageXpress Micro Confocal High Content Imaging System and HCS Studio cell analysis software (ThermoFisher). Images were captured with a 10x Nikon Plan Apo objective.

Photo-crosslinking methods—Details of the design and preparation of diazirine containing nucleosomes for photo-crosslinking studies will be described elsewhere (Dao et al., manuscript submitted). Briefly, diazirine-containing recombinant nucleosomes (0.5 uM) were incubated with biotinylated Cc peptides (12.5 uM) in binding buffer (20 mM HEPES, pH 7.9, 4mM Tris, pH 7.5, 150 mM KCl, 10 mM $MgCl_2$, 10% glycerol, and 0.02% (v/v) IGEPAL CA-630) at 30 °C for 30 mins, and cooled on ice for 5 mins. The reaction mixtures were then irradiated at 365 nm for 10 minutes. Reactions were then analyzed by western blotting employing IRDye® 800CW streptavidin on a LI-COR Odyssey Infrared Imager.

Recombinant Nucleosome Preparation (mutant nucleosome production)—Unmodified recombinant human histones (H2A, Uniprot ID: Q6FI13; H2B, Uniprot ID: O60814; H3C96A, C110A, Uniprot ID: P68431; H4, Uniprot ID: P62805), and histone mutants were produced in and purified from *E. coli* (Versteege et al. 1998). Histone octamers were prepared using established protocols (Luger et al. 1997). Nucleosomes were assembled as previously described with minor modifications (Luger et al. 1997). Briefly, a 601 DNA fragment was mixed with a similar volume of KCl (4M) to make a 2 M KCl mixture. Then, a histone octamer was added, and octamer refolding buffer (2 M NaCl, 10 mM Tris, 0.5 mM EDTA, 1 mM DTT, pH 7.8 at 4 °C) was used to adjusted final concentration of nucleosome to 0.5-1 μM. The mixture was placed in a Slide-A-Lyzer MINI dialysis unit (3.5 kDa MW cutoff, ThermoFisher Scientific) and dialyzed at 4 °C against 150 ml nucleosome assembly start buffer (10 mM Tris, 2 M KCl, 0.1 mM EDTA, 1 mM DTT, pH 7.5 at 4 °C) for 5 min at 4 °C. Subsequently, 450 ml nucleosome assembly end buffer (10 mM Tris, 10 mM KCl, 0.1 mM EDTA, 1 mM DTT, pH 7.5 at 4 °C) was added at a rate of 0.8 ml/min using a peristaltic pump to bring the overall KCl concentration to about 0.5 M. The dialysis mixture was then transferred to a microcentrifuge tube, incubated at 37 °C for 15 min, and centrifuged at 17,000×g for 10 m in. The supernatant was then transferred to a new dialysis unit and the mixture was dialyzed against nucleosome assembly end buffer twice (4 h each). After that, the dialysis mixture was transferred to a microcentrifuge tube, and centrifuged at 17,000×g for 10 min. Final nucleosome concentration was quantified by UV spectroscopy at 260 nm. The quality of individual nucleosomes was assessed by native polyacrylamide gel electrophoresis (5-6% acrylamide gel, 0.5× TBE, 150 V, 1 h), followed by SYBR® Gold DNA gel staining.

Circular Dichroism (CD)—Biotinylated peptides for analysis by CD were desalted using Pierce Peptide Desalting Spin Columns (ThermoFisher) following the manufacturer protocol. Peptides were eluted in 0.1% Trifluoroacetic acid (TFA) in 50% acetonitrile, lyophilized overnight, and re-dissolved in CD buffer (20 mM PO_4^-, pH 8) at 200 mM. Unbiotinylated peptides were dissolved directly in CD buffer at 200 mM. Single point CD

measurements were performed on an Aviv Model 430 CD Spectrometer using a 0.1 cm path length cell. Spectra were acquired at 25°C with a bandwidth of 1.0 nm, a scan rate of 100 nm/min, and averaging spectra over 10 scans.

SMARCB1-CTD Protein expression and purification: A construct of human SMARCB1, residues 351-385, in a pGEX-6P2 vector was transformed to E. coli BL21 (DE3) cells. In TB medium, cells were grown at 37°C in the presence of 100 μg/ml of ampicillin to an OD of 0.6, cooled to 17°C for 3 0 min, then induced with 500 μM isopropyl-1-thio-D-galactopyranoside. Induced culture was incubated overnight at 17°C, harvested by centrifugation and stored at −80°C. For 13C and 15N double-labeled SMARCB1, minimal media with appropriate substitution was used for expression, following the protocol adapted from reference (Marley, Lu, & Bracken, Journal of Biomolecular NMR). To purify SMARCB1-CTD, frozen cell pellets were resuspended in buffer-A (25 mM HEPES, pH 7.5, 200 mM NaCl, 5% glycerol, 1 mM EDTA, and 1 mM DTT) supplemented with 1 mM PMSF by stirring in cold room, lysed by Microfluidizer (Microfluidics), and the resulting lysate was centrifuged at 16,000 xg for 45 min. Glutathione sepharose beads (GE healthcare) were mixed with lysate supernatant for 90 min in rotating wheel and washed with buffer-A. Beads were transferred to an FPLC-compatible column and the bound protein was washed further with high salt buffer (buffer-A containing 1M NaCl), then buffer-A before eluting with buffer-A supplemented with 15mM glutathione. GST-3C protease was added to the eluted protein and incubated at 4°C overnight. Cleaved samples, confirmed by SDS-PAGE, were concentrated and purified by size exclusion chromatography using a Superdex 75 10/300 column (GE helathcare) equilibrated with buffer-A. SMARCB1 containing fractions were pooled, concentrated and frozen at −80°C.

NMR Methods—^{15}N and ^{13}C doubly-labeled SMARCB1-CTD, residues 351-385, protein were expressed from *E. coli* in M9 minimal medium containing ^{15}NH$_4$Cl and ^{13}C-gluocse as the sole nitrogen and carbon sources and purified as described above. Non-uniformly-sampled (NUS) triple resonance experiments, HNCA, HN(CO)CA, HNCO, HN(CA)CO, HN(CA)CB, C(CO)NH, H(CCO)NH and 15N-edited 3D-NOESY, using 0.3mM ^{15}N/^{13}C-SMARCB1CC protein in PBS buffer, pH 6.5 with 10% D$_2$O, were performed at 15°C on a 700 MHz Agilent DD2 spectrometer equipped with a cryogenic probe. 2D-NOESY and TOCSY spectra were acquired using an unlabeled sample in same buffer and 100% D2O on the same NMR spectrometer. The data were processed using NMRPipe (Delaglio et al., 1995) and Iterative Soft Thresholding reconstruction approach (istHMS) (Hyberts et al., 2012) and analyzed by CARA (Keller et al., 2004). Backbone dihedral angle restraints and secondary structure predications based on assigned chemical shifts were obtained using the TALOS+ software (Shen et al., 2009). Fifty structural model with 422 NOE distance restraints and 15 identified hydrogen-bonds were calculated using the XPLOR-NIH software (Schwieters et al., 2003), from which 10 lowest energy SMARCB1-CTD conformers are selected for deposition in the Protein DataBank database (PDB ID: 6UCH).

Proteomics—A 10 μL aliquot of concentrated HA-purified mSWI/SNF complexes described above were run on a 4-12% Bis-Tris SDS PAGE gel and stained with Colloidal

Blue (Colloidal Blue Staining Kit, Invitrogen) following the NuPAGE Novex Bis-Tris gel staining kit protocol. mSWI/SNF gel bands were excised from the gel and submitted Harvard Univeristy's Taplin Mass Spectrometry Facility for processing.

Flow Cytometry—Cells were analyzed following the protocol for the Abcam Annexin V-CF Blue 7-AAD Apoptosis Staining/Detection Kit (ab214663). Briefly, 100,000 cells were washed twice in room temperature PBS and resuspended in 1x Binding Solution. 5uL of Annexin V-CF Blue conjugate and 5uL of 7-AAD staining solution were added and incubated for 15 minutes at room temperature, at which time 400uL of 1x Binding Solution was added. Cells were analyzed on a LSR Fortessa (BD biosciences). Data was analyzed using FlowJo software (v.10.4.1, TreeStar).

ChIP preparation and protocol—ChIP-seq was performed using standard protocols (Millipore, Billerica, MA). Specifically, cells were fixed in 1% formaldehyde (Sigma Aldrich, F8775) for 10 min at 37°C and quenched with 125 mM glycine for 5 min at 37°C. After washing, nuclei were sonicated using Covaris Sonicator, and the supernatant was used for immunoprecipitation with the indicated antibody (Table S2). ChIP-sequencing libraries were prepared with Illumina's NEBNext Ultra II DNA library Prep Kit using standard protocols. All ChIP-seq was sequenced on Illumina Next-seq 500 using 75 bp single-end sequencing parameters.

RNA isolation and preparation—All RNA was collected in duplicate and isolated using the RNeasy Mini Kit (QIAGEN) according to manufacturer's protocol. RNA-seq libraries were prepared with Illumina's TruSeq standard mRNA Sample Prep Kit using standard protocols. All RNA was sequenced on Illumina Next-seq 500 (Illumina) using 75 bp single-end sequencing parameters through Dana-Farber Cancer Institute's Molecular Biology Core Genomics Facility.

ATAC-seq protocol—ATAC-seq libraries were prepared using 50,000 cells per sample following a standard protocol (Mashtalir et al. 2018) with 12 cycles of amplification. ATAC-seq samples were sequenced on Next-seq 500 (Illumina) using 37 bp pair-end sequencing parameters.

MNase-seq preparation—One million cells per condition were treated with 0.5 U of Micrococcal Nuclease (MNase, Zymo, Cat# D5220-1) using the EZ Nucleosomal DNA Prep Kit (Zymo, Cat# D5220) following the kit protocol. Size fractionation of MNase-digested DNA was performed using a 2% Agarose gel cassette (Sage Science, Cat# CSD2010) and run on a Pippin Prep machine (Sage Science) to obtain DNA between 120-180 bps. Appropriate size distribution of MNase-digested DNA was confirmed using a D1000 Screentape (Agilent Technologies) run on a 2200 TapeStation System (Agilent Technologies). Library preparation of MNase-digested DNA was carried using the NEBNext Ultra II DNA Library Prep Kit for Illumina (New England Biolabs, Cat# E7645). Paired-End 50 next generation sequencing was performed using a NovaSeq 6000 (Illumina) through Dana-Farber Cancer Institute's Molecular Biology Core Genomics Facility.

QUANTIFICATION AND STATISTICAL ANALYSIS

Sequence data processing and acquisition—RNAseq, ChIPseq, and ATACseq samples were sequenced with the Illumina NextSeq 500 technology, and MNase-seq samples were sequenced with the Illumina NovaSeq technology. Output data were demultiplexed using the bcl2fastq software tool. RNAseq reads were aligned to the hg19 genome with STAR v2.5.2b (Pan et al. 2018), and ChIPseq reads were aligned with Bowtie2 v2.29 in the −k 1 reporting mode (Pan et al. 2018; Mashtalir et al. 2018; Michel et al. 2018). For the ATACseq and MNase-seq data, quality read trimming was performed by Trimmmomatic v0.36 (Diets et al. 2018; Kleefstra et al. 2012), followed by alignment, duplicate read removal, and read quality filtering using Bowtie2 v2.29, Picard v2.8.0 (Liu et al. 2017), and SAMtools v0.1.19 (Lupas et al. 1991), respectively. For the ChIPseq, ATACseq, and MNase-seq data, output BAM files were converted into BigWig track files using BEDTools (Sen et al. 2017; Dutta et al. 2017) and UCSC utilities (Phelan et al. 1999; Nakayama et al. 2017; Wang et al. 2017) in order to display coverage throughout the genome. For the RNAseq data, tracks were generated using the deepTools v2.5.3 bamCoverage function (Dann et al. 2017). These data have been deposited at NCBI's Gene Expression Omnibus under accession number GSE124903. TTC1240 SS18, ARID2, H3K4me1, and H3K4me3 ChIP-seq data were acquired from GSE90634 (Yingsha Zhang et al. 2013). HUES64 OCT4, NANOG, and SOX2 ChiP-seq data were obtained from GSE61475 (Yingsha Zhang et al. 2013).

RNA-seq data analysis—For the RNA-seq data, output gene count tables from STAR based on alignments to the hg19 reflat annotation were used as input into edgeR v3.12.1 (Nakayama et al. 2017) to evaluate differential gene expression. Log2 fold change values from edgeR were used as input into GSEA (Singhal et al. 2010), and the GseaPreranked tool was run with default settings to measure gene set enrichment. In order analyze gene ontology and pathway enrichment for select subsets of genes, Metascape was used (Tripathi et al. 2015). RpKm values were quantified using median length isoforms and total mapped read counts computed by the Samtools idxstats function. Principle Components Analysis was performed using the wt.scale and fast.svd functions from the corpcor R package on RPKM values (Schäfer & Strimmer 2005) (Opgen-Rhein & Strimmer 2007).

ATAC-seq, MNase-seq, and ChIP-seq data analysis—For the ChIP-seq data, narrow peaks were called with the MACS2 v2.1.1 software (Yong Zhang et al. 2008) using input as controls and a q-value cutoff of 0.001, and for the ATAC-seq data, broad peaks were called with MACs using the BAMPE option with a broad peak cutoff of 0.001. The R package, ChIPpeakAnno v3.17.0, was used to perform peak overlap analyses, and cis-regulatory function was assessed by GREAT (McLean et al. 2010). To evaluate differential accessibility between the WT and K364del conditions, raw read counts from ATAC-seq samples within ATAC-seq peaks were computed using the BEDTools intersect function, and these counts were used as input into edgeR. For the MNase-seq data, fragment length distributions were derived from properly-paired read alignments in output SAM files. Metaplots and heat maps were generated using ngsplot v2.63 (Shen et al. 2014). Transcription factor enrichment and motif analysis were carried out by the LOLA v1.12.0 (Sheffield & Bock 2016) and HOMER v4.9 (Heinz et al. 2010) software packages, respectively.

Supplementary Material

Refer to Web version on PubMed Central for supplementary material.

Acknowledgements

References

Ashkenazy H, Abadi S, Martz E, Chay O, Mayrose I, Pupko T, and Ben-Tal N (2016). ConSurf 2016: an improved methodology to estimate and visualize evolutionary conservation in macromolecules. Nucl. Acids Res. 44, W344–W350. [PubMed: 27166375]

Barisic D, Stadler MB, Iurlaro M, Schübeler D (2019). Mammalian ISWI and SWI/SNF selectively mediate binding of distinct transcription factors. Nature 569, 136–140. [PubMed: 30996347]

Bögershausen N, and Wollnik B (2018). Mutational Landscapes and Phenotypic Spectrum of SWI/SNF-Related Intellectual Disability Disorders. Front Mol Neurosci 11, 252. [PubMed: 30123105]

Bolger AM, Lohse M, and Usadel B (2014). Trimmomatic: a flexible trimmer for Illumina sequence data. Bioinformatics 30, 2114–2120. [PubMed: 24695404]

Buenrostro JD, Wu B, Chang HY, and Greenleaf WJ (2015). ATAC-seq: A Method for Assaying Chromatin Accessibility Genome-Wide. Current Protocols in Molecular Biology 21.29.1–21.29.9.

Cairns BR, Kim YJ, Sayre MH, Laurent BC, and Kornberg RD (1994). A multisubunit complex containing the SWI1/ADR6, SWI2/SNF2, SWI3, SNF5, and SNF6 gene products isolated from yeast. Proceedings of the National Academy of Sciences 91, 1950–1954.

Clapier CR, and Cairns BR (2009). The biology of chromatin remodeling complexes. Annu. Rev. Biochem. 78, 273–304. [PubMed: 19355820]

Dann GP, Liszczak GP, Bagert JD, Muller MM, Nguyen UTT, Wojcik F, Brown ZZ, Bos J, Panchenko T, Pihl R, et al. (2017). ISWI chromatin remodellers sense nucleosome modifications to determine substrate preference. Nature 548, 607–611. [PubMed: 28767641]

Dechassa ML, Zhang B, Horowitz-Scherer R, Persinger J, Woodcock CL, Peterson CL, and Bartholomew B (2008). Architecture of the SWI/SNF-nucleosome complex. Mol. Cell. Biol. 28, 6010–6021. [PubMed: 18644858]

Delaglio F et al. NMRPipe: A multidimensional spectral processing system based on UNIX pipes. J. Biomol. NMR 6,277–293 (1995). [PubMed: 8520220]

Diets IJ, Prescott T, Champaigne NL, Mancini GMS, Krossnes B, Fri R, Kocsis K, Jongmans MCJ, and Kleefstra T (2018). A recurrent de novo missense pathogenic variant in SMARCB1 causes

severe intellectual disability and choroid plexus hyperplasia with resultant hydrocephalus. Genetics in Medicine 2018 69, 1.

Dobin A, Davis CA, Schlesinger F, Drenkow J, Zaleski C, Jha S, Batut P, Chaisson M, and Gingeras TR (2013). STAR: ultrafast universal RNA-seq aligner. Bioinformatics 29, 15–21. [PubMed: 23104886]

Dsouza, Zimmermann, & Gedes, A case of Coffin-Siris Syndrome with severe congenital heart disease and a novel SMARCA4 variant. CSH Molecular Case Studies (2019)

Dutta A, Sardiu M, Gogol M, Gilmore J, Zhang D, Florens L, Abmayr SM, Washburn MP, and Workman JL (2017). Composition and Function of Mutant Swi/Snf Complexes. Cell Reports 18, 2124–2134. [PubMed: 28249159]

Ebrahimi-Fakhari et al., Impaired Mitochondrial Dynamics and Mitophagy in Neuronal Models of Tuberous Sclerosis Complex. Cell Reports (2016)

Forbes SA, Beare D, Boutselakis H, Bamford S, Bindal N, Tate J, Cole CG, Ward S, Dawson E, Ponting L, et al. (2017). COSMIC: somatic cancer genetics at high-resolution. Nucl. Acids Res. 45, D777–D783. [PubMed: 27899578]

Forbes SA, Bindal N, Bamford S, Cole C, Kok CY, Beare D, Jia M, Shepherd R, Leung K, Menzies A, et al. (2011). COSMIC: mining complete cancer genomes in the Catalogue of Somatic Mutations in Cancer. Nucl. Acids Res. 39, D945–D950. [PubMed: 20952405]

Gao F Elliot NJ, Ho J, Sharp A, Shokhirev MN, and Hargreaves DC, Heterozygous Mutations in SMARCA2 Reprogram the Enhancer Landscape by Global Retargeting of SMARCA4. Mol Cell 75, 891–904.e7 (2019). [PubMed: 31375262]

Guntert P Automated structure determination from NMR spectra. Eur Biophys J. 38(2), 129–143 (2009). [PubMed: 18807026]

Heinz S, Benner C, Spann N, Bertolino E, Lin YC, Laslo P, Cheng JX, Murre C, Singh H, and Glass CK (2010). Simple combinations of lineage-determining transcription factors prime cis-regulatory elements required for macrophage and B cell identities. Mol Cell 38, 576–589. [PubMed: 20513432]

Hyberts SG, Milbradt AG, Wagner AB, Arthanari H & Wagner G Application of iterative soft thresholding for fast reconstruction of NMR data non-uniformly sampled with multidimensional Poisson Gap scheduling. J. Biomol. NMR 52, 315–327 (2012). [PubMed: 22331404]

Kadoch C, and Crabtree GR (2015). Mammalian SWI/SNF chromatin remodeling complexes and cancer: Mechanistic insights gained from human genomics. Sci Adv 1, e1500447–e1500447. [PubMed: 26601204]

Kadoch C, Hargreaves DC, Hodges C, Elias L, Ho L, Ranish J, and Crabtree GR (2013). Proteomic and bioinformatic analysis of mammalian SWI/SNF complexes identifies extensive roles in human malignancy. Nat Genet 45, 592–601. [PubMed: 23644491]

Kalpana GV, Marmon S, Wang W, Crabtree GR, and Goff SP (1994). Binding and stimulation of HIV-1 integrase by a human homolog of yeast transcription factor SNF5. Science 266, 2002–2006. [PubMed: 7801128]

Keller R Optimizing the process of nuclear magnetic resonance spectrum analysis and computer aided resonance assignment. Swiss Fed. Inst. Technol. Zurich (2004).

Kleefstra T, Kramer JM, Neveling K, Willemsen MH, Koemans TS, Vissers LE, Wissink-Lindhout W, Fenckova M, van den Akker WM, Kasri NN, et al. (2012). AR TICLE Disruption of an EHMTI-Associated Chromatin- Modification Module Causes Intellectual Disability. The American Journal of Human Genetics 91, 73–82. [PubMed: 22726846]

Kosho T, Miyake N, and Carey JC (2014a). Coffin-Siris syndrome and related disorders involving components of the BAF (mSWI/SNF) complex: Historical review and recent advances using next generation sequencing. Am. J. Med. Genet. 166, 241–251.

Kosho T, Okamoto N, Coffin-Siris Syndrome International Collaborators (2014b). Genotype-phenotype correlation of Coffin-Siris syndrome caused by mutations in SMARCB1, SMARCA4, SMARCE1, and ARID1A. Am. J. Med. Genet 166C, 262–275. [PubMed: 25168959]

Kuhn RM, Haussler D, and Kent WJ (2013). The UCSC genome browser and associated tools. Brief. Bioinformatics 14, 144–161. [PubMed: 22908213]

Kwon CS, and Wagner D (2007). Unwinding chromatin for development and growth: a few genes at a time. Trends Genet. 23, 403–412. [PubMed: 17566593]

Langmead B, and Salzberg SL (2012). Fast gapped-read alignment with Bowtie 2. Nat Meth 9, 357–359.

Liu X, Li M, Xia X, Li X, and Chen Z (2017). Mechanism of chromatin remodelling revealed by the Snf2-nucleosome structure. Nature 544, 440–445. [PubMed: 28424519]

Luger K, Rechsteiner TJ, Flaus AJ, Waye MM, and Richmond TJ (1997). Characterization of nucleosome core particles containing histone proteins made in bacteria. Journal of Molecular Biology 272, 301–311. [PubMed: 9325091]

Lupas A, Van Dyke M, and Stock J (1991). Predicting coiled coils from protein sequences. Science 252, 1162–1164. [PubMed: 2031185]

Mannino EA, Miyawaki H, Santen G, and Schrier Vergano SA (2018). First data from a parent-reported registry of 81 individuals with Coffin-Siris syndrome: Natural history and management recommendations. Am. J. Med. Genet. 176, 2250–2258. [PubMed: 30276971]

Mashtalir N, Daou S, Barbour H, Sen NN, Gagnon J, Hammond-Martel I, Dar HH, Therrien M, and Affar EB (2014). Autodeubiquitination Protects the Tumor Suppressor BAP1 from Cytoplasmic Sequestration Mediated by the Atypical Ubiquitin Ligase UBE2O. Mol Cell 54, 392–406. [PubMed: 24703950]

Mashtalir N, D'Avino AR, Michel BC, Luo J, Pan J, Otto JE, Zullow HJ, McKenzie ZM, Kubiak RL, St Pierre R, et al. (2018). Modular Organization and Assembly of SWI/SNF Family Chromatin Remodeling Complexes. Cell.

Marley J, Lu M & Bracken C J Biomol NMR (2001) 20: 71 10.1023/A:1011254402785 [PubMed: 11430757]

McLean CY, Bristor D, Hiller M, Clarke SL, Schaar BT, Lowe CB, Wenger AM, and Bejerano G (2010). GREAT improves functional interpretation of cis-regulatory regions. Nat Biotechnol 28, 495–501. [PubMed: 20436461]

Michel BC, D'Avino AR, Cassel SH, Mashtalir N, McKenzie ZM, McBride MJ, Valencia AM, Zhou Q, Bocker M, Soares LMM, et al. (2018). A non-canonical SWI/SNF complex is a synthetic lethal target in cancers driven by BAF complex perturbation. Nat. Cell Biol 154, 490–1420.

Miyake N, Tsurusaki Y, and Matsumoto N (2014). Numerous BAF complex genes are mutated in Coffin-Siris syndrome. Am. J. Med. Genet 166C, 257–261. [PubMed: 25081545]

Nakayama RT, Pulice JL, Valencia AM, McBride MJ, McKenzie ZM, Gillespie MA, Ku WL, Teng M, Cui K, Williams RT, et al. (2017). SMARCB1 is required for widespread BAF complex-mediated activation of enhancers and bivalent promoters. Nat Genet 49, 1613–1623. [PubMed: 28945250]

Nemani L, Barik R, Patnaik AN, Mishra RC, Rao AM, Kapur P. Coffin-Siris syndrome with the rarest constellation of congenital cardiac defects: A case report with review of literature. Ann Pediatr Cardiol. 2014;7(3):221–226. doi:10.4103/0974-2069.140859 [PubMed: 25298701]

Opgen-Rhein R, and Strimmer K (2007). Accurate ranking of differentially expressed genes by a distribution-free shrinkage approach. Stat Appl Genet Mol Biol 6, Article9.

Pan J, Meyers RM, Michel BC, Mashtalir N, Sizemore AE, Wells JN, Cassel SH, Vazquez F, Weir BA, Hahn WC, et al. (2018). Interrogation of Mammalian Protein Complex Structure, Function, and Membership Using Genome-Scale Fitness Screens. Cell Systems 6, 555–568.e557. [PubMed: 29778836]

Pan J McKenzie ZM, D'Avino AR, Mashtalir N, Lareau CA, St. Pierre R, Wang L, Shilatifard A, and Kadoch C (2019). The ATPase module of mammalian SWI/SNF complexes mediates subcomplex identity and catalytic activity-independent genomic targeting. Nat Genet 51, 618–626. [PubMed: 30858614]

Peterson CL, Zhao Y, and Chait BT (1998). Subunits of the yeast SWI/SNF complex are members of the actin-related protein (ARP) family. Journal of Biological Chemistry 273, 23641–23644. [PubMed: 9726966]

Phelan ML, Sif S, Narlikar GJ, and Kingston RE (1999). Reconstitution of a core chromatin remodeling complex from SWI/SNF subunits. Mol Cell 3, 247–253. [PubMed: 10078207]

Picard. Available at: http://broadinstitute.github.io/picard/ (Accessed: 15 February 2019)

Ronan JL, Wu W, and Crabtree GR (2013). From neural development to cognition: unexpected roles for chromatin. Nat Rev Genet 14, 347–359. [PubMed: 23568486]

Quinlan AR, and Hall IM (2010). BEDTools: a flexible suite of utilities for comparing genomic features. Bioinformatics 26, 841–842. [PubMed: 20110278]

Ramírez F, Ryan DP, Grüning B, Bhardwaj V, Kilpert F, Richter AS, Heyne S, Dündar F, and Manke T (2016). deepTools2: a next generation web server for deep-sequencing data analysis. Nucl. Acids Res 44, W160–W165. [PubMed: 27079975]

Robinson MD, McCarthy DJ, and Smyth GK (2010). edgeR: a Bioconductor package for differential expression analysis of digital gene expression data. Bioinformatics 26, 139–140. [PubMed: 19910308]

Santen GWE, Aten E, Sun Y, Almomani R, Gilissen C, Nielsen M, Kant SG, Snoeck IN, Peeters EAJ, Hilhorst-Hofstee Y, et al. (2012). Mutations in SWI/SNF chromatin remodeling complex gene ARID1B cause Coffin-Siris syndrome. Nat Genet 44, 379–380. [PubMed: 22426309]

Santen GWE, Aten E, Vulto-van Silfhout AT, Pottinger C, van Bon BWM, van Minderhout IJHM, Snowdowne R, van der Lans CAC, Boogaard M, Linssen MML, et al. (2013). Coffin-Siris Syndrome and the BAF Complex: Genotype-Phenotype Study in 63 Patients. Human Mutation 34, 1519–1528. [PubMed: 23929686]

Santen GWE, Kriek M, and van Attikum H (2014). SWI/SNF complex in disorder. Epigenetics 7, 1219–1224.

Schäfer J, and Strimmer K (2005). A shrinkage approach to large-scale covariance matrix estimation and implications for functional genomics. Stat Appl Genet Mol Biol 4, Article32.

Schmitz U, Mueller W, Weber M, Sévenet N, Delattre O, and Deimling von, A. (2001). INI1 mutations in meningiomas at a potential hotspot in exon 9. Br. J. Cancer 84, 199–201. [PubMed: 11161377]

Schwieters CD, Kuszewski JJ, Tjandra N and Clore GM The Xplor-NIH NMR Molecular Structure Determination Package. J. Magn. Res, 160, 66–74 (2003).

Sen P, Luo J, Hada A, Hailu SG, Dechassa ML, Persinger J, Brahma S, Paul S, Ranish J, and Bartholomew B (2017). Loss of Snf5 Induces Formation of an Aberrant SWI/SNF Complex. Cell Reports 18, 2135–2147. [PubMed: 28249160]

Sheffield NC, and Bock C (2016). LOLA: enrichment analysis for genomic region sets and regulatory elements in R and Bioconductor. Bioinformatics 32, 587–589. [PubMed: 26508757]

Shen L, Shao N, Liu X, and Nestler E (2014). ngs.plot: Quick mining and visualization of next-generation sequencing data by integrating genomic databases. BMC Genomics 15, 284. [PubMed: 24735413]

Shen Y, Delaglio F, Cornilescu G & Bax A TALOS+: A hybrid method for predicting protein backbone torsion angles from NMR chemical shifts. J. Biomol. NMR 44, 213–23 (2009). [PubMed: 19548092]

Sheridan SD, Theriault KM, Reis SA, Zhou F, Madison JM, Daheron L, Loring JF, and Haggarty SJ Epigenetic characterization of the FMR1 gene and aberrant neurodevelopment in human induced pluripotent stem cell models of fragile X syndrome. Plos One, 6, e26203 (2011). [PubMed: 22022567]

Singhal N, Graumann J, Wu G, Araúzo-Bravúo MJ, Han DW, Greber B, Gentile L, Mann M, and Schöler HR (2010). Chromatin-Remodeling Components of the BAF Complex Facilitate Reprogramming. Cell 141, 943–955. [PubMed: 20550931]

Sokpor G, Xie Y, Rosenbusch J, and Tuoc T (2017). Chromatin Remodeling BAF (SWI/SNF) Complexes in Neural Development and Disorders. Front Mol Neurosci 10, 243. [PubMed: 28824374]

Subramanian A, Tamayo P, Mootha VK, Mukherjee S, Ebert BL, Gillette MA, Paulovich A, Pomeroy SL, Golub TR, Lander ES, et al. (2005). Gene set enrichment analysis: A knowledge-based approach for interpreting genome-wide expression profiles. Proc. Natl. Acad. Sci. U. S. a 102, 15545–15550. [PubMed: 16199517]

Tate JG, Bamford S, Jubb HC, Sondka Z, Beare DM, Bindal B, Boutselakis H, Cole CG, Creatore C, Dawson E, et al., COSMIC: the Catalogue Of Somatic Mutations In Cancer, Nucleic Acids Research, Volume 47, Issue D1, 08 1 2019, Pages D941–D947, 10.1093/nar/gky1015 [PubMed: 30371878]

Tiscornia G, Singer O, and Verma IM (2006). Production and purification of lentiviral vectors. Nat Protoc 1, 241–245. [PubMed: 17406239]

Tripathi S, Pohl MO, Zhou Y, Rodriguez-Frandsen A, Wang G, Stein DA, Moulton HM, DeJesus P, Che J, Mulder LCF, et al. (2015). Meta- and Orthogonal Integration of Influenza "OMICs" Data Defines a Role for UBR4 in Virus Budding. Cell Host Microbe 18, 723–735. [PubMed: 26651948]

Tsankov AM, Gu H, Akopian V, Ziller MJ, Donaghey J, Amit I, Gnirke A, and Meissner A (2015). Transcription factor binding dynamics during human ES cell differentiation. Nature 518, 344–349. [PubMed: 25693565]

Tsurusaki Y, Okamoto N, Ohashi H, Mizuno S, Matsumoto N, Makita Y, Fukuda M, Isidor B, Perrier J, Aggarwal S, et al. (2013). Coffin-Siris syndrome is a SWI/SNF complex disorder. Clinical Genetics 85, 548–554. [PubMed: 23815551]

Tsurusaki Y, Okamoto N, Ohashi H, Kosho T, Imai Y, Hibi-Ko Y, Kaname T, Naritomi K, Kawame H, Wakui K, et al. (2012). Mutations affecting components of the SWI/SNF complex cause Coffin-Siris syndrome. Nat Genet 44, 376–378. [PubMed: 22426308]

Versteege I, Sévenet N, Lange J, Rousseau-Merck MF, Ambros P, Handgretinger R, Aurias A, and Delattre O (1998). Truncating mutations of hSNF5/INI1 in aggressive paediatric cancer. Nature 394, 203–206. [PubMed: 9671307]

Vissers LELM, Gilissen C, and Veltman JA (2016). Genetic studies in intellectual disability and related disorders. Nat Rev Genet 17, 9–18. [PubMed: 26503795]

Wang W, Xue Y, Zhou S, Kuo A, Cairns BR, and Crabtree GR (1996). Diversity and specialization of mammalian SWI/SNF complexes. Genes Dev. 10, 2117–2130. [PubMed: 8804307]

Wang X, Lee RS, Alver BH, Haswell JR, Wang S, Mieczkowski J, Drier Y, Gillespie SM, Archer TC, Wu JN, et al. (2017). SMARCB1-mediated SWI/SNF complex function is essential for enhancer regulation. Nat Genet 49, 289–295. [PubMed: 27941797]

Wieczorek D, Bogershausen N, Beleggia F, Steiner-Haldenstatt S, Pohl E, Li Y, Milz E, Martin M, Thiele H, Altmuller J, et al. (2013). A comprehensive molecular study on Coffin-Siris and Nicolaides-Baraitser syndromes identifies a broad molecular and clinical spectrum converging on altered chromatin remodeling. Human Molecular Genetics 22, 5121–5135. [PubMed: 23906836]

Workman JL, and Kingston RE (1998). Alteration of nucleosome structure as a mechanism of transcriptional regulation. Annu. Rev. Biochem 67, 545–579. [PubMed: 9759497]

Zhang Y, Pak C, Han Y, Ahlenius H, Zhang Z, Chanda S, Marro S, Patzke C, Acuna C, Covy J, et al. (2013). Rapid Single-Step Induction of Functional Neurons from Human Pluripotent Stem Cells. Neuron 78, 785–798. [PubMed: 23764284]

Zhang Y, Liu T, Meyer CA, Eeckhoute J, Johnson DS, Bernstein BE, Nusbaum C, Myers RM, Brown M, Li W, et al. (2008). Model-based analysis of ChIP-Seq (MACS). Genome Biol. 9, R137. [PubMed: 18798982]

Highlights

A conserved SMARCB1 C-terminal alpha helix binds the nucleosome acidic patch

Recurrent point mutations disrupt this interaction and mSWI/SNF nucleosome remodeling

The SMARCB1 CTD is dispensable for BAF complex targeting genome-wide

Heterozygous SMARCB1 mutations impede Ngn2-mediated neuronal differentiation
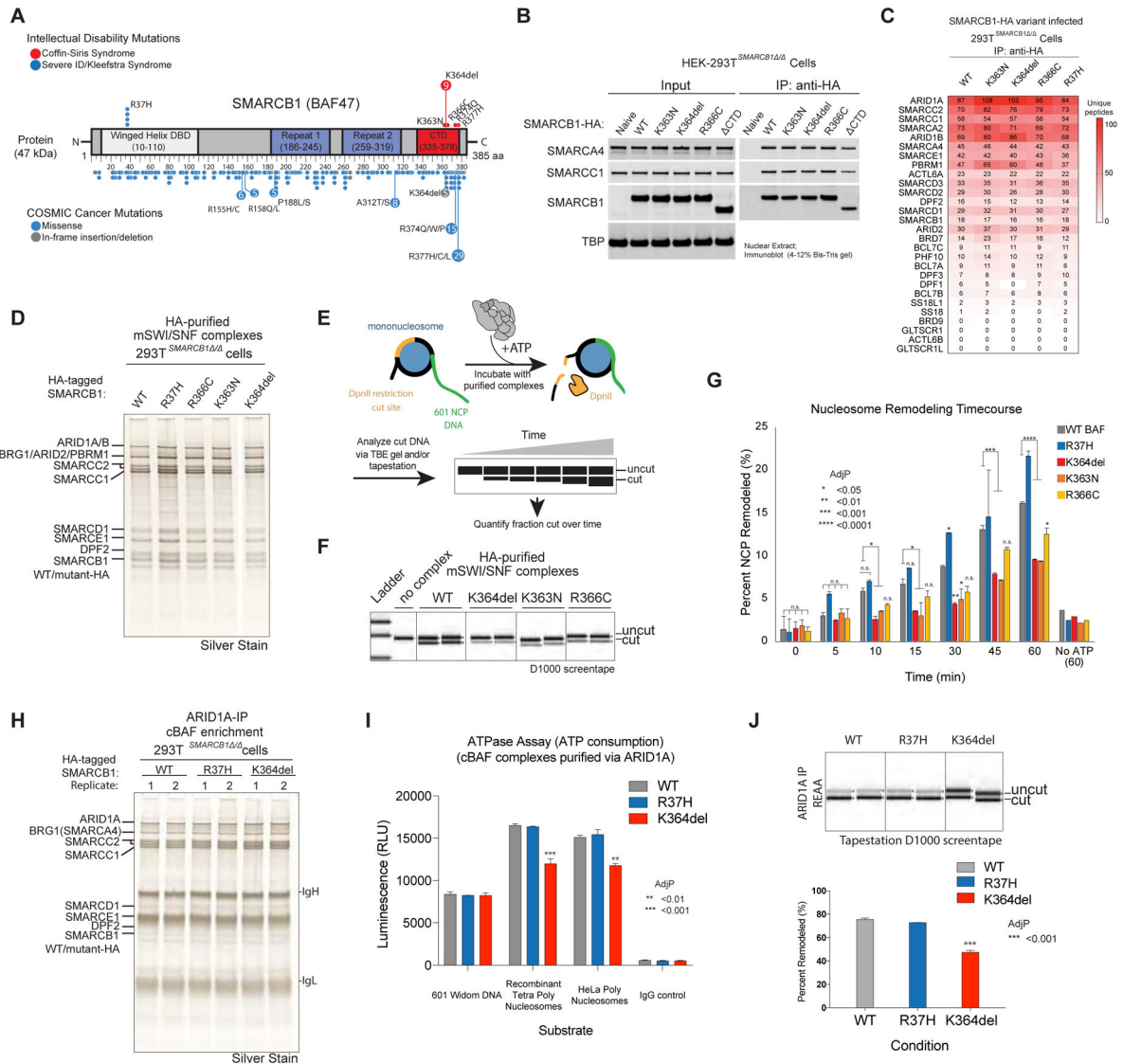
Figure 1. CSS-associated mutations in the SMARCB1 CTD inhibit mSWI/SNF nucleosome remodeling and ATPase activity on nucleosomes.

A. Summary of missense mutations and in-frame deletions in SMARCB1-associated intellectual disability (ID) syndromes (Coffin-Siris syndrome, Kleefstra syndrome, and non-syndromic severe ID), and cancer (COSMIC). Legends are indicated.

B. Immunoblot performed on total nuclear protein and anti-HA immunoprecipitations in SMARCB1-deficient HEK-293T cells.

C. Proteomic mass spectrometry results of 293T-SMARCB1 knockout 293Ts expressing WT or mutant SMARCB1 constructs.

D. HA-epitope purification of HA-tagged SMARCB1 WT and mutant variant-bound complexes from SMARCB1-deficient HEK-293T cells. Silver staining confirms capture of expected mSWI/SNF subunits and their stoichiometry (superfluous lane deletion separated by white line).

E. Schematic for restriction enzyme accessibility assay (REAA) with ST601-GATC1 nucleosome core particle (NCP) harboring a DpnII restriction cut site used to assess nucleosome remodeling of purified mSWI/SNF complexes.

F. Nucleosome remodeling (REAA) comparing SMARCB1 WT and mutant variant complexes visualized by Tapestation D1000 (200 ng purified complexes, 30 °C, 90 min).

G. Summary of nucleosome remodeling assay using REAA comparing all SMARCB1 WT and mutant variants over time course (200 ng purified complexes, 30 °C, 0-60 minutes, mean ± S.D., n=2; AdjP-values determined by Dunnett's multiple comparison test compared to WT at each time point).

H. Endogenous ARID1A-IP of SMARCB1 WT- and mutant variant- bound complexes.

I. ATPase assays performed on mSWI/SNF complexes via ARID1A IP (for canonical BAF complexes from (H)) in solution with 601 Widom DNA, recombinant tetra polynucleosomes, or HeLa polynucleosomes (30 °C, 90 min). Luminescence signal is plotted (mean ± S.D., n=2; AdjP-values determined by Dunnett's multiple comparison test to WT for each substrate).

J. REAA remodeling assay performed in parallel to (I) with recombinant mononucleosomes. See also Figure S1, Table S1, and Table S2.
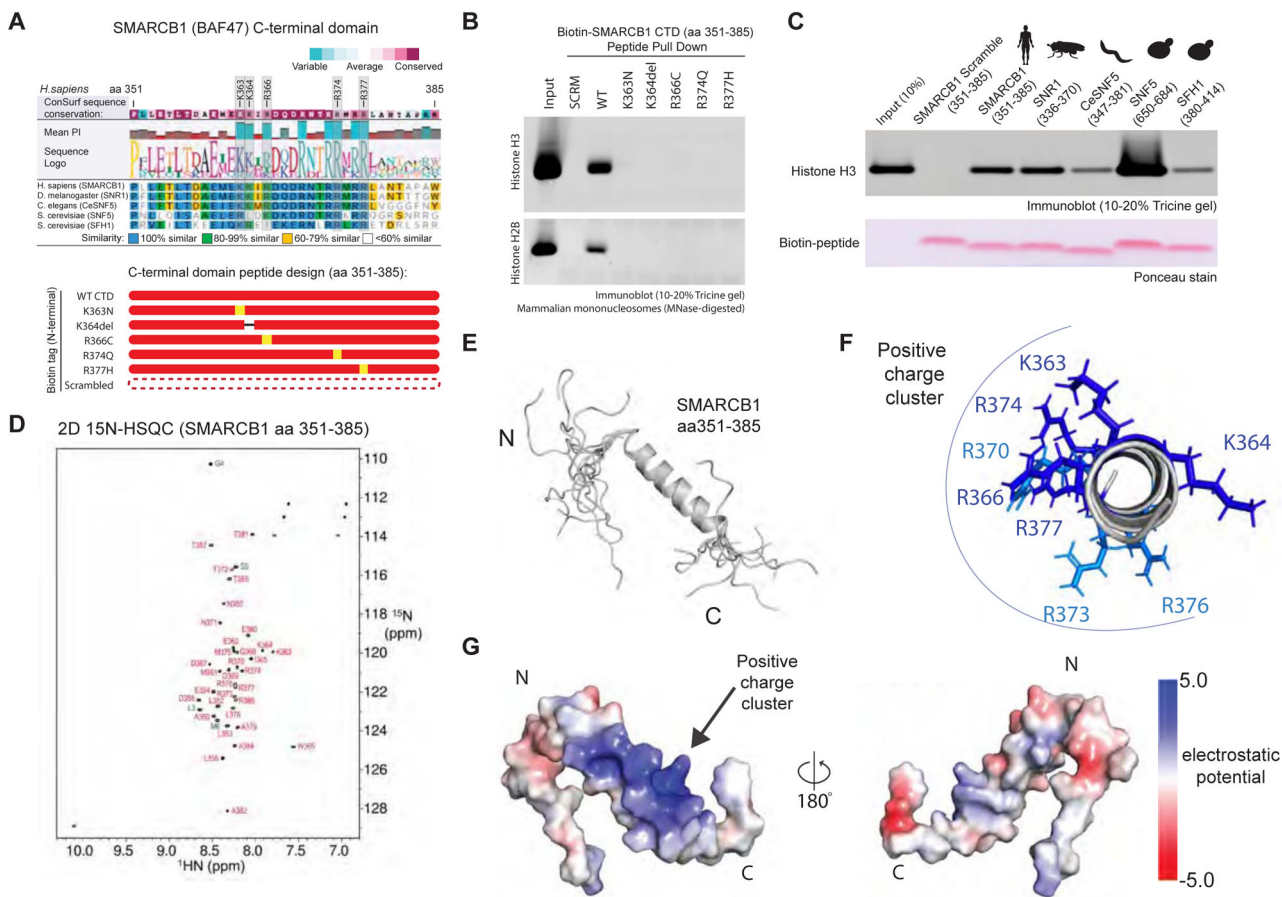
Figure 2. The SMARCB1 CTD binds directly to nucleosomes, mediated by a basic, alpha-helical amino acid cluster.

A. Top, conservation of minimal SNF5 homology putative c-terminal domains across species showing ConSurf conservation score, mean pI, sequence logo, and similarity. CSS-associated mutated residues are highlighted in gray. Bottom, N-terminally biotinylated SMARCB1-CTD peptide (aa 351-385) variants generated.

B. H. sapiens SMARCB1 CTD WT and mutant intellectual disability-associated biotin-tagged peptide pull downs of mammalian mononucleosomes; immunoblot for histone H3 and histone H2B.

C. Immunoblot of peptide pull down of mammalian mononucleosomes across SMARCB1-CTD homologues (*H. sapiens* SMARCB1 scramble and wild-type, *D. melanogaster* SNR1, *C. elegans* CeSNF5, or *S. cerevisiae* SNF5 and SFH1).

D. Backbone assignment. 2D 15N-HSQC spectrum of 0.5 mM 15N-SMARCB1-CTD in PBS, pH 6.5 acquired at 15°C. The backbone NH peaks from SMARCB1-CC residues are assigned in red, and residues from N-terminal cloning tag are assigned in blue.

E. Superposition of backbone traces of the 10 lowest-energy structures of the SMARCB1 c-terminal domain (aa 351-385).

F. Barrel view cartoon diagram of a representative structure from the of SMARCB1 c-terminal alpha helix highlighting CSS mutated residues in dark blue and additional positive (Arg/Lys) residues in light blue (aa 357-378).

G. Electrostatic surface potential of the SMARCB1-CTD, calculated using ABPS (Dolinsky et al., 2004), from −5.0 kTE^-1 (red) to +5.0 kTE^-1 (blue). 180 degree rotations are shown. See also Figure S2 and Table S3.
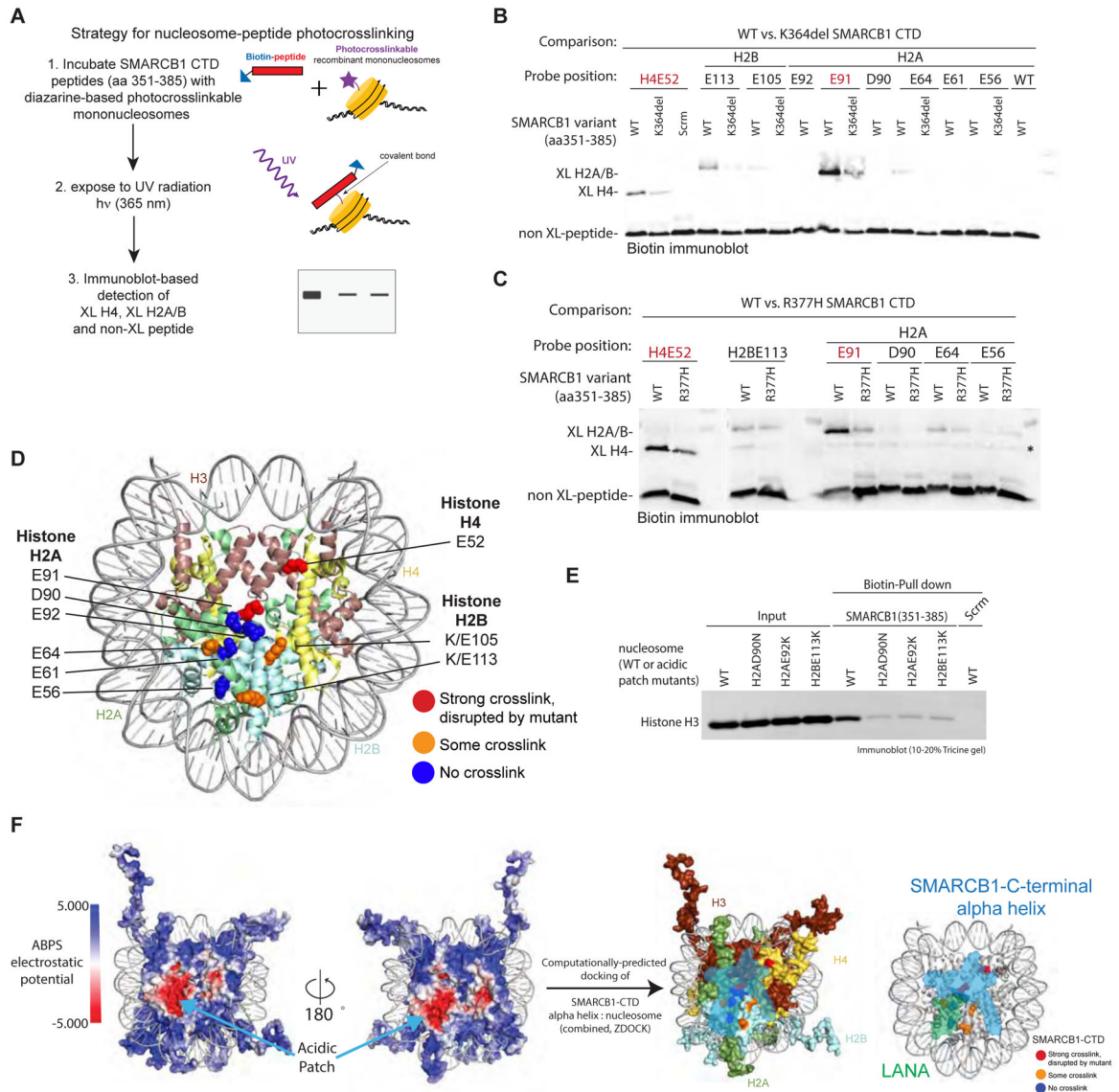
Figure 3. The SMARCB1 CTD binds to the nucleosome acidic patch, which is disrupted by CSS-associated missense mutations.

A. Assay schematic for photocrosslinking-based assessment of SMARCB1 CTD binding sites with photocrosslinkable histone residues.

B-C. SDS-PAGE immunoblots for biotin resolving Histones H2A/B and H4 as well as non-XL peptide across acidic patch residues for WT and mutant SMARCB1 CTD peptides.

D. Summary of crosslinking results within the nucleosome acidic patch (PDB ID: 1ZLA).

E. WT SMARCB1 CTD peptide pull-down of WT and acidic patch mutant recombinant mononucleosomes.

F. (left) Electrostatic potential of nucleosome (PDB ID: 1KX5) with acidic patch highlighted, with 180 degree rotations; and (right) ZDOCK predicted docking region of SMARCB1-CTD (aa 358-377) on nucleosome overlaid in light blue (compiled across binding constraints) (Pierce et al., 2014). H2A-green, H2B-cyan, H3-maroon, H4-yellow. See also Figure S3.
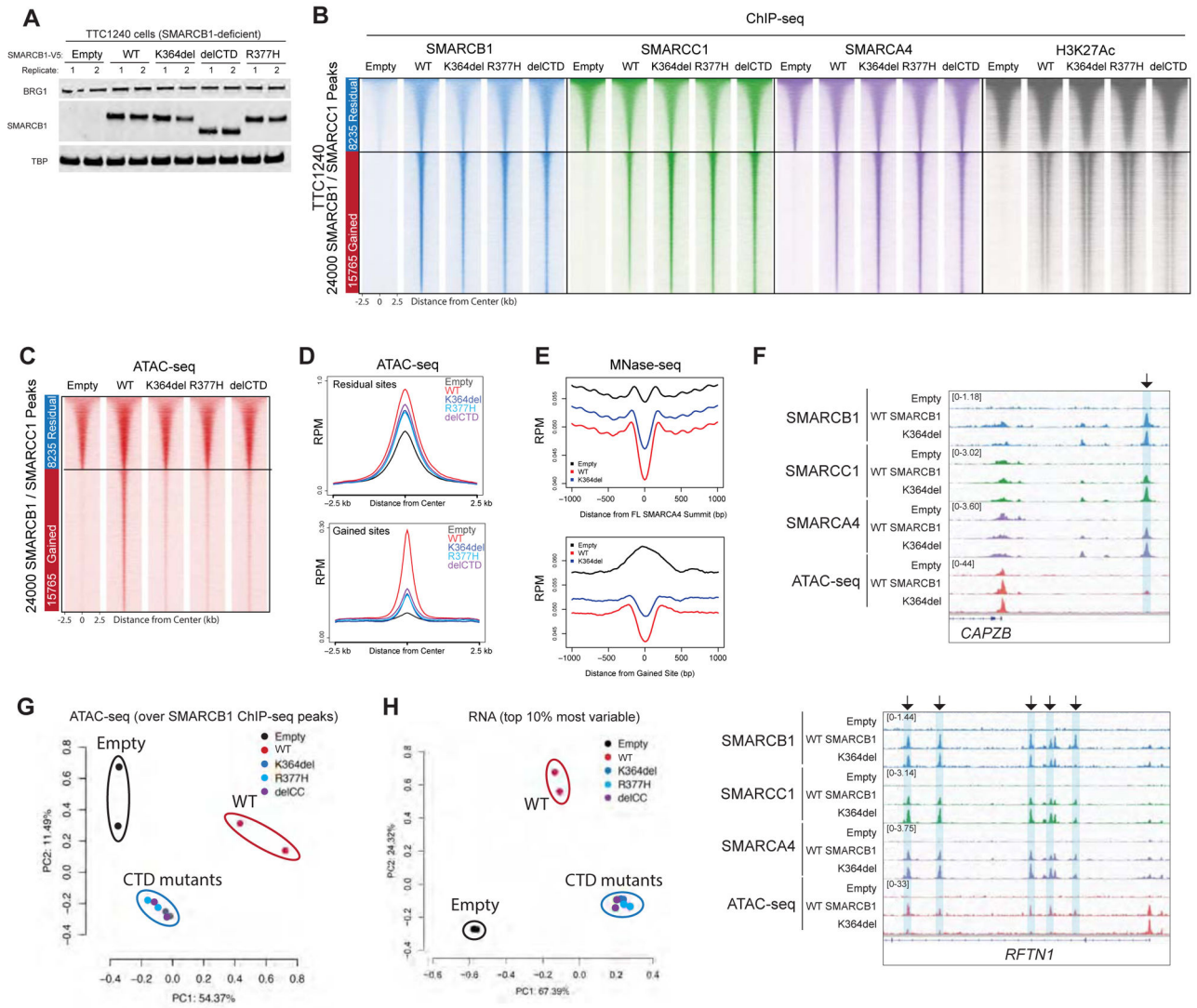
Figure 4. CSS-associated mutations in SMARCB1 disrupt genome-wide enhancer DNA accessibility without affecting mSWI/SNF complex targeting.

A. Introduction of C-terminal V5-tagged SMARCB1 WT and mutant variants in TTC1240 SMARCB1-deficient MRT cells. Immunoblot for BRG1, SMARCB1, and TBP are shown.

B. Chromatin occupancy of mSWI/SNF complexes (marked by SMARCB1, SMARCC1, and SMARCA4) and H3K27Ac occupancy mapped over overlapped merged SMARCB1/ SMARCC1 peaks.

C. Heatmap of ATAC-seq genomic accessibility reads over residual and de novo sites.

D. Summary metaplots reflecting accessibility at residual (top) and gained (bottom) sites for empty vector, SMARCB1 WT, and SMARCB1 CTD mutant conditions.

E. Metaplot of MNase-seq over all SMARCA4 WT summits (top) and gained mSWI/SNF sites.

F. Example ChIP-seq and ATAC-seq tracks over the CAPZB (top) and RTFN1 (bottom) loci.

G. Principal component analysis (PCA) performed on ATAC-seq peaks overlapping SMARCB1 ChIP-seq sites; experimental replicates for empty vector, SMARCB1 WT, and SMARCB1 CTD mutant conditions.

H. PCA performed on RNA-seq experimental replicates for empty vector, SMARCB1 WT, and SMARCB1 CTD mutant conditions (top 10% most variable genes).

See also Figure S4.
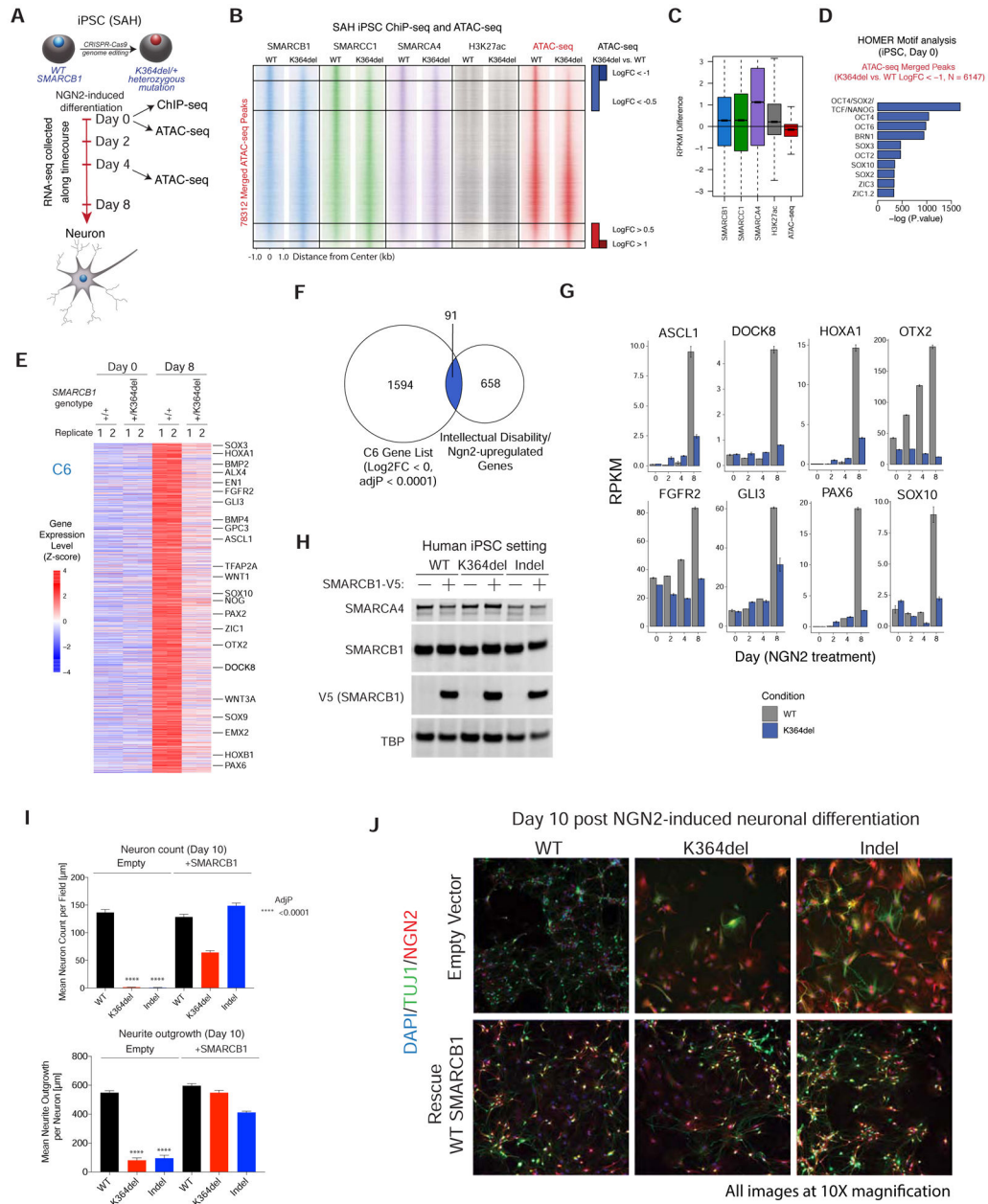
Figure 5. CSS-associated heterozygous SMARCB1 mutations in iPSCs block neuronal differentiation.

A. CRISPR-Cas9 mediated genome editing was used to obtain heterozygous SMARCB1 K364del and indel mutant iPSCs which underwent NGN2-mediated neuronal differentiation with RNA-seq collected along an 8 day timecourse for WT and K364del mutant cells.

B. Heatmap of ChIP-seq for mSWI/SNF subunits (SMARCB1, SMARCC1, SMARCA4) and H3K27ac as well as ATAC-seq of SMARCB1 +/+ and K364del/+ iPSCs.

C. Box plot of normalized difference between WT and K364del/+ mutant SMARCB1, SMARCC1, SMARCA4, H3K27ac ChIP-seq and ATAC-seq results.

D. HOMER motif analysis of sites with reduced ATAC-seq accessibility (from B) in the K364del mutant versus WT iPSCs.

E. Heatmap of gene cluster downregulated in K364del versus WT cells at Day 8 of NGN2-induced differentiation (Cluster 6). Select differentially regulated genes are highlighted. See also Figure S5I

F. Venn diagram depicting overlap of Cluster 6 genes with intellectual disability- and NGN2-induced differentiation- associated genes.

G. Bar graphs of intellectual-disability associated genes downregulated in the mutant versus wild-type cells along the differentiation time course.

H. Immunoblot demonstrating lentiviral expression of full-length V5-tagged SMARCB1 in WT and mutant iPSCs.

I. Neurite outgrowth and neuron count at Day 10 of NGN2 differentiation (mean ± S.E.M, n=12; AdjP-values determined by Dunnett's multiple comparison test to WT(EV)).

J. Imaging of DAPI (DNA), TUJ1, and NGN2 in SAH iPSCs at day 10 of differentiation.

K. Model of genome-wide localization and activity of mSWI/SNF complexes assembled with WT or CSS-associated SMARCB1 mutant variants.

See also Figure S5 and Table S4.
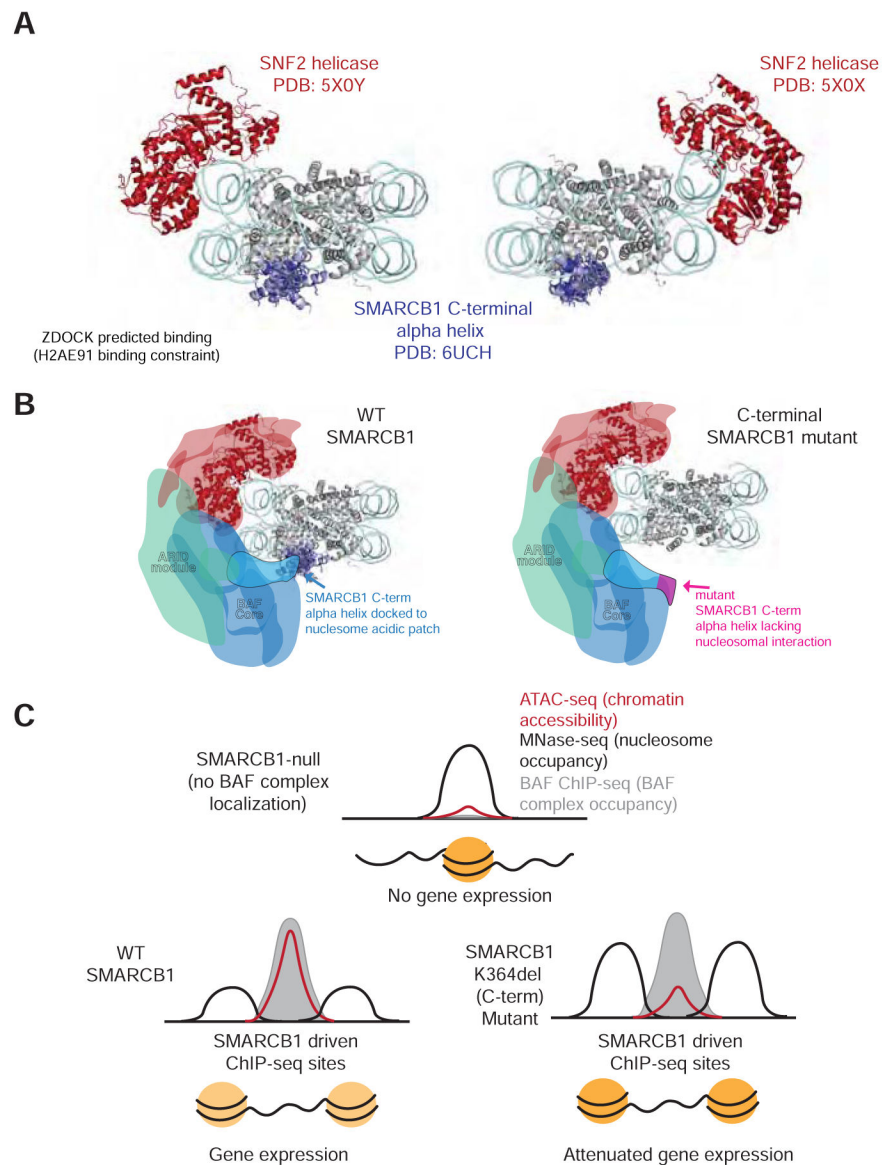
Figure 6. Model of SMARCB1-mediated nucleosome engagement and remodeling.
A. Model of SMARCB1 C-terminal alpha helix bound to nucleosomes in complex with SNF2h bound (left) at the SHL2 position (PDB ID: 5X0Y) and (right) at the SHL6 nucleosomal position (PDB ID: 5X0X) generated using ZDOCK (H2AE91 binding constraint).

B. Model of mammalian SWI/SNF complex based on Mashtalir et al. with WT or C-terminal mutant SMARCB1 subunit as part of core module.

C. Model of genome-wide BAF complex occupancy (ChIP-seq), chromatin accessibility (ATAC-seq), nucleosome occupancy (MNase-seq) and gene expression between SMARCB1-null, WT, and C-terminal mutant conditions at SMARCB1-driven BAF complex sites.

KEY RESOURCES TABLE

REAGENT or RESOURCE	SOURCE	IDENTIFIER
Antibodies		
Mouse Anti-SMARCC2 (BAF170) (G-12) (WB)	Santa Cruz	Cat# sc-166237, Lot: G1310; RRID: AB_2192013
Mouse Anti-SMARCD1 (BAF60A) (23) (WB)	Santa Cruz	Cat# sc-135843, Lot: A2616; RRID: AB_2192137
Rabbit Anti-PBRM1(BAF180) (WB)	Millipore	Cat# ABE70, Lot: A2616; RRID: AB_10807561
Rabbit Anti-SMARCE1 (BAF57) (WB)	Bethyl	Cat# A300-810A, Lot: 2; RRID: AB_577243
Mouse Anti-TATA binding protein (TBP) (WB)	Abcam	Cat# ab51841, Lot: GR297600-4; RRID: AB_945758
Rabbit Anti-Histone H3 (WB)	Abcam	Cat# ab1791, Lot: GR3236377-1; RRID: AB_302613
Rabbit Anti-Histone H2B (D2H6) (WB)	Cell Signaling Technology	Cat# 12364, RRID: AB_2714167
Rabbit Anti-PARP (WB)	Cell Signaling Technology	Cat# 9532, Lot: 9; RRID: AB_659884
Rabbit Anti-Cleaved PARP (Asp214) XP (WB)	Cell Signaling Technology	Cat# 5625, Lot: 13; RRID: AB_10699459
Mouse Anti-IgG (IP)	Santa Cruz	Cat# sc-2025, Lot: H0615; RRID: AB_737182
Rabbit Anti-ARID1A (BAF250A) (D2A8U) (IP/WB)	Cell Signaling Technology	Cat# 12354, Lot: 1; RRID: AB_2637010
Mouse Anti-Anti-INI1 (BAF47) (A-5) (IP/WB) (IP/WB)	Santa Cruz	Cat# sc-166165, Lot: K0515; RRID: AB_2270651
Mouse Anti-Anti-BRG1 (SMARCA4) (G-7) (IP/WB)	Santa Cruz	Cat# sc-17796, Lot: G0115; RRID: AB_626762
Rabbit Anti-HA-Tag (C29F4) (IP/WB) (ChIP/WB)	Cell Signaling Technology	Cat# 3724S, Lot: 8; RRID: AB_1549585
Rabbit Anti-SMARCB1 (BAF47) (D8M1X) (ChIP/WB)	Cell Signaling Technology	Cat# 91735, Lot: 1; RRID: AB_2800172
Rabbit Anti-SMARCC1 (BAF155) (D7F8S) (ChIP/WB)	Cell Signaling Technology	Cat# 11956, Lot: 2; RRID: AB_2797776
Rabbit Anti-SMARCA4 (BRG1) (EPNCIR111A) (ChIP)	Abcam	Cat# ab110641, Lot: GR150844-37*, Lot: GR3208604-7**; RRID: AB_10861578
Rabbit Anti-Histone H3 (acetyl K27)-ChIP Grade (ChIP)	Abcam	Cat# ab4729, Lot: GR238071-2*, Lot: GR144577-1**; RRID: AB_2118291
Mouse Anti-RNA Pol II monoclonal antibody – Classic (ChIP)	Diagenode	Cat# C15200004, Lot: 001-11; RRID: AB_2728744
Rabbit Anti-SUZ12 (D39F6) XP (ChIP)	Cell Signaling	Cat# 3737, Lot: 6; RRID: AB_2196850
Rabbit Anti-H3K27me3 (trimethyl Histone H3 (Lys27)) (ChIP)	Millipore	Cat# 07-449, Lot: 2275589; RRID: AB_310624

REAGENT or RESOURCE	SOURCE	IDENTIFIER
Mouse Anti-Beta-Tubulin III (TUJ1) (IF)	Sigma-Aldrich	Cat# T8660, RRID: AB_477590
Goat Anti-Mouse IgG Antibody, IRDye 680RD Conjugated	LI-COR Biosciences	Cat# 926-68070, RRID: AB_10956588
Goat Anti-Rabbit IgG Antibody, IRDye 800CW Conjugated	LI-COR Biosciences	Cat# 926-32211, RRID: AB_621843
Note: Asterisks denote whether antibody was used for ChIP for either *-TTC1240 or **-SAH iPSC cell line.		
Bacterial and Virus Strains		
One-Shot Stbl 3 chemically competent cells	Invitrogen	Cat# C7373-03
Rosetta (DE3) Competent Cells	Novagen	Cat# 70954
BL21 (DE3) Competent E. coli	New England Biolabs	Cat# C2527H
Biological Samples		
MNase-digested purified mononucleosomes from 293T cells	This study, protocol adapted from Masthalir et al., Mol Cell 2014	N/A
HeLa Polynucleosomes Purified	EpiCypher	Cat# 16-0003
Chemicals, Peptides, and Recombinant Proteins		
Peptide: Biotin-SMARCB1_SCRM (351-385): Bio-TENTKLDLMRIPENKLARATRWRQTDLEARPMDAR (35-mer)	KE Biochem	N/A
Peptide: Biotin-SMARCB1_WT (351-385): Bio-PLLETLTDAEMEKKIRDQDRNTRRMRRLANTAPAW (35-mer)	KE Biochem	N/A
Peptide: Biotin-SMARCB1_K364del (351-385): Bio-PLLETLTDAEMEKIRDQDRNTRRMRRLANTAPAW (34-mer)	KE Biochem	N/A
Peptide: Biotin-SMARCB1_R377H (351-385): Bio-PLLETLTDAEMEKKIRDQDRNTRRMRHLANTAPAW (35-mer)	KE Biochem	N/A
Peptide: Biotin-SMARCB1_R366C (351-385): Bio-PLLETLTDAEMEKKICDQDRNTRRMRRLANTAPAW (35-mer)	KE Biochem	N/A
Peptide: Biotin-SMARCB1_K363N (351-385): Bio-PLLETLTDAEMENKIRDQDRNTRRMRRLANTAPAW (35-mer)	KE Biochem	N/A
Peptide: Biotin-SMARCB1_R374Q (351-385): Bio-PLLETLTDAEMEKKIRDQDRNTRQMRRLANTAPAW (35-mer)	KE Biochem	N/A
Peptide: Biotin-SMARCB1_K364A (351-385): Bio-PLLETLTDAEMEKAIRDQDRNTRRMRRLANTAPAW (35-mer)	KE Biochem	N/A
Peptide: Biotin-SMARCB1_K364E (351-385): Bio-PLLETLTDAEMEKEIRDQDRNTRRMRRLANTAPAW (35-mer)	KE Biochem	N/A
Peptide: Biotin-SMARCB1_K364R (351-385): Bio-PLLETLTDAEMEKRIRDQDRNTRRMRRLANTAPAW (35-mer)	KE Biochem	N/A
Peptide: Biotin-SMARCB1_K364P (351-385): Bio-PLLETLTDAEMEKPIRDQDRNTRRMRRLANTAPAW (35-mer)	KE Biochem	N/A
Peptide: Biotin-SMARCB1_I365A (351-385): Bio-PLLETLTDAEMEKKARDQDRNTRRMRRLANTAPAW (35-mer)	KE Biochem	N/A
Peptide: Biotin-SMARCB1_AA-363/4 (351-385): Bio-PLLETLTDAEMEAAIRDQDRNTRRMRRLANTAPAW (35-mer)	KE Biochem	N/A
Peptide: Biotin-SMARCB1_EE-363/4 (351-385): Bio-PLLETLTDAEMEEEIRDQDRNTRRMRRLANTAPAW (35-mer)	KE Biochem	N/A
Peptide: Biotin-SMARCB1_K363A (351-385): Bio-PLLETLTDAEMEAKIRDQDRNTRRMRRLANTAPAW (35-mer)	KE Biochem	N/A
Peptide: Biotin-SMARCB1_R370A (351-385): Bio-PLLETLTDAEMEKKIRDQDANTRRMRRLANTAPAW (35-mer)	KE Biochem	N/A

REAGENT or RESOURCE	SOURCE	IDENTIFIER
Peptide: Biotin-S.cerevisae_SNF5_WT (650-684): Bio-PNLLQISAAELERLDKDKDRDTRRKRRQGRSNRRG (35-mer)	KE Biochem	N/A
Peptide: Biotin-S.cerevisae_SFH1_WT (380-414): Bio-PRVEILTKEEIQKREIEKERNLRRLKRETDRLSRR (35-mer)	KE Biochem	N/A
Peptide: Biotin-C.elegans_SNF5_WT (347-381): Bio-PFLETLTDAEIEKKMRDQDRNTRRMRRLVGGGFNY (35-mer)	KE Biochem	N/A
Peptide: Biotin-D.melanogaster_SNR1_WT (336-370): Bio-PFLETLTDAEMEKKIRDQDRNTRRMRRLANTTTGW (35-mer)	KE Biochem	N/A
Peptide: Biotin-SMARCB1_WT (351-382): Bio-PLLETLTDAEMEKKIRDQDRNTRRMRRLANTA (32-mer)	KE Biochem	N/A
Peptide: Biotin-SMARCB1_K364del (351-382): Bio-PLLETLTDAEMEKKIRDQDRNTRRMRRLANTA (31-mer)	KE Biochem	N/A
Peptide: SMARCB1_WT (351-382): PLLETLTDAEMEKKIRDQDRNTRRMRRLANTA (32-mer) (CD)	KE Biochem	N/A
Peptide: SMARCB1_K364del (351-382): PLLETLTDAEMEKKIRDQDRNTRRMRRLANTA (31-mer) (CD)	KE Biochem	N/A
Peptide: SMARCB1_R377H (351-382): PLLETLTDAEMEKKIRDQDRNTRRMRHLANTA (32-mer) (CD)	KE Biochem	N/A
Peptide: SMARCB1_R366C (351-382): PLLETLTDAEMEKKICDQDRNTRRMRRLANTA (32-mer) (CD)	KE Biochem	N/A
Peptide: SMARCB1_K363N (351-382): PLLETLTDAEMENKIRDQDRNTRRMRRLANTA (32-mer) (CD)	KE Biochem	N/A
Peptide: SMARCB1_R374Q (351-382): PLLETLTDAEMEKKIRDQDRNTRQMRRLANTA (32-mer) (CD)	KE Biochem	N/A
Peptide: LANA Peptide (1-23): MAPPGMRLRSGRSTGAPLTRGSC (23-mer)	KE Biochem	N/A
15N-Ammonium Chloride	Cambridge Isotope	Cat# NLM-467-1
13C-glucose	Cambridge Isotope	Cat# CLM-1396-2
Ponceau S Staining Solution	Sigma Aldrich	Cat# P7170
Dynabeads Streptavidin	Thermo Fisher Scientific	Cat# 88817
Dynabeads Protein G	Thermo Fisher Scientific	Cat# 10004D
Pierce Anti-HA Magnetic Beads	Thermo Fisher Scientific	Cat# 88837
Puromycin	Sigma-Aldrich	Cat# P8833-25MG
Blasticidin	Life Technologies	Cat# R210-01
Polybrene	Santa Cruz Biotechnology	Cat# sc-134220
Polyethylenimine (PEI) (MW 40,000)	Polysciences	Cat# 24765
Formaldehyde	Sigma-Aldrich	Cat# F8775
Glycine	Sigma-Aldrich	Cat# G7126
RNase	Roche	Cat#11119915001
Proteinase K Solution	Thermo Fisher Scientific	Cat# AM2546
MNase	Sigma-Aldrich	Cat# N3755
Agencourt AMPure XP Beads	Beckman Coulter	Cat# A63882
High Sensitivity D1000 ScreenTape & Reagents	Agilent	Cat# 5067-5584/5585
High Sensitivity D5000 ScreenTape & Reagents	Agilent	Cat# 5067-5592/5593

REAGENT or RESOURCE	SOURCE	IDENTIFIER
Recombinant mononucleosome with diazirine photocrosslinker at Histone H4E52	Laboratory of Dr. Thomas W. Muir, Princeton University	N/A
Recombinant mononucleosome with diazirine photocrosslinker at Histone H2BE113	Laboratory of Dr. Thomas W. Muir, Princeton University	N/A
Recombinant mononucleosome with diazirine photocrosslinker at Histone H2BE105	Laboratory of Dr. Thomas W. Muir, Princeton University	N/A
Recombinant mononucleosome with diazirine photocrosslinker at Histone H2AE91	Laboratory of Dr. Thomas W. Muir, Princeton University	N/A
Recombinant mononucleosome with diazirine photocrosslinker at Histone H2AD90	Laboratory of Dr. Thomas W. Muir, Princeton University	N/A
Recombinant mononucleosome with diazirine photocrosslinker at Histone H2AE64	Laboratory of Dr. Thomas W. Muir, Princeton University	N/A
Recombinant mononucleosome with diazirine photocrosslinker at Histone H2AE61	Laboratory of Dr. Thomas W. Muir, Princeton University	N/A
Recombinant mononucleosome with diazirine photocrosslinker at Histone H2AE56	Laboratory of Dr. Thomas W. Muir, Princeton University	N/A
Recombinant Mononucleosome: Wild-type	Laboratory of Dr. Thomas W. Muir, Princeton University	N/A
Recombinant Mononucleosome: Mutant-Histone H2AD90N	Laboratory of Dr. Thomas W. Muir, Princeton University	N/A
Recombinant Mononucleosome: Mutant-Histone H2AE92K	Laboratory of Dr. Thomas W. Muir, Princeton University	N/A
Recombinant Mononucleosome: Mutant-Histone H2BE113K	Laboratory of Dr. Thomas W. Muir, Princeton University	N/A
EpiDyne Nucleosome Remodeling Assay Substrate ST601-GATC1	EpiCypher	Cat# 16-4101
Recombinant tetranucleosomes	Reaction Biology	Cat# HMT-15-369
Recombinant histone octamer	EpiCypher	Cat#16-0001
6X GelPilot Loading Dye	QIAGEN	Cat# 239901
DpnII Restriction Enzyme	New England Biolabs	Cat# R0543L
Ultrapure ATP (provided in ADP Glo Max Assay kit)	Promega	Cat# V7001
Recombinant ^{15}N/^{13}C doubly-labeled SMARCB1-C-terminal protein (aa 351-385)	This study, Dana-Faber Cancer Institute Structural Biology Core	N/A
Recombinant SMARCB1-WH DNA binding domain	Purification adapted from Allen at al., Structure 2015	N/A
Cycloheximide	Sigma-Aldrich	Cat# C1988-1G
SYBR-Gold Nucleic Acid Gel Stain	Thermo Fisher Scientific/Invitrogen	Cat# S11494
SYBR-Safe Nucleic Acid Gel Stain	Thermo Fisher Scientific/Invitrogen	Cat# S33102

REAGENT or RESOURCE	SOURCE	IDENTIFIER
Syto-60 Red Fluorescent Nucleic Acid Stain	Thermo Fisher Scientific/Invitrogen	Cat# S11342
IRDye 800CW Streptavidin for Biotin Detection	LI-COR Biosciences	Cat# 926-32230
StemFlex™ Medium	Thermo Fisher Scientific/Gibco	Cat# A3349401
ReLeSR™ Enzyme-free human ES and iPS cell selection and passaging reagent	Stem Cell Technologies	Cat# 05872
CryoStor® CS1 Freeze Media	Bio Life Solutions	Cat# 210102
Critical Commercial Assays		
NEBNext Ultra II DNA Library Prep Kit for Illumina	New England Biolabs	Cat# E7645
NextSeq 500/550 High Output Kit v2.5 (75 Cycles)	Illumina	Cat# 20024906
NovaSeq 6000 SP Reagent Kit (100 cycles)	Illumina	Cat# 20027464
EZ Nucleosomal DNA Prep Kit	Zymo Research	Cat# D5220
RNEasy Mini Kit	Qiagen	Cat# 74136
MinElute PCR Purification Kit	Qiagen	Cat# 28006
ADP-Glo Max Assay	Promega	Cat# V7001
2% Agarose w/ external markers, Pippin Prep. 100-600 bp	Sage Science	Cat# CSD2010
BCA Protein Assay Kit	Pierce/ Thermo Scientific	Cat# 23225
SilverQuest Silver Staining Kit	Invitrogen	Cat# LC6070
Annexin V-CF Blue 7-AAD Apoptosis Staining/Detection Kit	Abcam	Cat# ab214663
Deposited Data		
TTC1240 ChIP-seq, RNA-seq, ATAC-seq, MNase-seq; G401 RNA-seq; SAH ChIP-seq, RNA-seq, ATAC-seq	This study	GEO: GSE124903
TTC1240 SS18, ARID2, H3K4me1, and H3K4me3 ChIP-seq	Nakayama et al., Nat. Gen. 2017	GEO: GSE90634
HUES64 OCT4, NANOG, and SOX2 ChIP-seq data	Tsankov et al., Nature 2015	GEO: GSE61475
NMR Structure of SMARCB1 C-Terminal Alpha Helix	This study	PDB: 6UCH
X-Ray Structure of the Nucleosome Core Particle	Davey et al., J. Mol. Biol. 2002	PDB: 1KX5
X-ray Structure of a Kaposi's sarcoma herpesvirus LANA peptide bound to the nucleosomal core	Chodaparambil et al., Science 2006	PDB: 1ZLA
Complex of Snf2-Nucleosome complex with Snf2 bound to positions SHL2 and SHL6 of the nucleosome	Liu et al., Nature 2017	PDB: 5X0X; 5X0Y
Experimental Models: Cell Lines		
Lenti-X 293T cell line	Clontech	Cat# 632180; RRID: CVCL_4401
HEK293T$^{SMARCB1\ /}$ (293T BAF47KO (29.1)) cell line	Nakayama et al., Nat. Gen. 2017	N/A
TTC1240	Gift from laboratory of Dr. T.J. Triche, Children's Hospital Los Angeles (CHLA)	RRID: CVCL_8002
G401	ATCC	RRID: CVCL_0270
SAH (SAH0047-2)	Ebrahimi-Fakhari et al., Cell Rep. 2016	N/A

REAGENT or RESOURCE	SOURCE	IDENTIFIER
SAH*SMARCB1*_K364del/+	This study	N/A
SAH*SMARCB1*_Indel/+	This study	N/A
Experimental Models: Organisms/Strains		
N/A	N/A	N/A
Oligonucleotides		
SMARCB1-K364del sgRNA, 5'-GGAGAAGAAGATCCGCGACC **AGG**-3'	Integrated DNA Technologies	N/A
SMARCB1-K364del ssODN, 5'- CCGGAACACG GGCGATGCGG ACCAGTGGTG CCCACTGCTG GAGACTCTGA CAGACGCTGA GATGGAA-**A**--A**A**T**A**CGCG **A**TC**AA**GACAG GAACACGAGG TACCCCTGGC CCTGTGGTCC TGGGCTCTGC CCACAGGCAC CTGGCTTTCC -3';	Integrated DNA Technologies	N/A
INI1 Winged Helix DNA Binding DNA (5' IRDye700-GGAATTGTGAGCGCTCACAATTCC-3')	Integrated DNA Technologies, Adapted from Allen et al., 2015	N/A
INI1 Winged Helix DNA Binding DNA (unlabeled reverse complement) (5'-GGAATTGTGAGCGCTCACAATTCC-3')	Integrated DNA Technologies, Allen et al., 2015	N/A
Recombinant DNA		
EF-1a-MCS-PGK-Blast (Empty Vector)	Clonetech, Kadoch & Crabtree (2013)	N/A
EF-1a-MCS-PGK-Blast-SMARCB1-V5 WT	Nakayama et al., 2017	N/A
EF-1a-MCS-PGK-Blast-SMARCB1-V5 K364del	This study	N/A
EF-1a-MCS-PGK-Blast-SMARCB1-V5 R377H	This study	N/A
EF-1a-MCS-PGK-Blast-SMARCB1-V5 delCC (Y326*)	This study	N/A
EF-1a-MCS-PGK-Blast-SMARCB1-V5 delN-term (deletion of aa 1-176)	This study	N/A
EF-1a-MCS-PGK-Blast-SMARCB1-V5 delC-term (deletion of aa 177-385)	This study	N/A
EF-1a-MCS-PGK-Blast-SMARCB1-V5 delRpt1 (deletion of aa 186-245)	This study	N/A
EF-1a-MCS-PGK-Blast-SMARCB1-V5 delRpt2 (deletion of aa 259-319)	This study	N/A
EF-1a-MCS-PGK-Blast-SMARCB1-V5 delRpt1-2 (deletion of aa 186-319)	This study	N/A
EF-1a-MCS-PGK-Puro (Empty Vector)	Clonetech, Kadoch & Crabtree (2013)	N/A
EF-1a-MCS-PGK-Puro-SMARCB1-HA WT	This study	N/A
EF-1a-MCS-PGK-Blast-SMARCB1-HA R37H	This study	N/A
EF-1a-MCS-PGK-Blast-SMARCB1-HA K364del	This study	N/A
EF-1a-MCS-PGK-Blast-SMARCB1-HA K363N	This study	N/A
EF-1a-MCS-PGK-Blast-SMARCB1-HA R366C	This study	N/A
psPAX2	Tiscornia et al., 2006	RRID: Addgene_12260
pMD2.G	Tiscornia et al., 2006	RRID: Addgene_12259
Ini1 (BAF47) CRISPR/Cas9 KO Plasmid	Santa Cruz Biotechnology	Cat# sc-423027
Ini1 (BAF47) HDR Plasmid	Santa Cruz Biotechnology	Cat# sc-423027-HDR
pSpCas9(BB)-2A-GFP (PX458) CRISPR/Cas9 Plasmid constructed with hSMARCB1 distinct sgRNA (see Olignonucleotides above)	Ran et al., 2013	RRID: Addgene_48138
pGEX-6P-2-SMARCB1CC (aa 351-385)	This study	N/A

REAGENT or RESOURCE	SOURCE	IDENTIFIER
pGST-SMARCB1WH (aa 1-115)	This study adapted from Allen at al., Structure 2015	N/A
Software and Algorithms		
Bowtie2 v2.29	Langmead and Sialzberg, 2012	http://bowtie-bio.sourceforge.net/bowtie2/index.shtml ; RRID:SCR_005476
STAR v2.5.2b	Dobin et al., 2013	https://github.com/alexdobin/STAR ; RRID:SCR_015899
MAC2 v2.1.1	Zhang et al., 2008	https://github.com/taoliu/MACS ; RRID:SCR_013291
GSEA	Subramanian et al., 2005	http://software.broadinstitute.org/gsea/index.jsp ; RRID:SCR_003199
BEDTools	Quinlan and Hall, 2010	http://bedtools.readthedocs.io/en/latest/ ; RRID:SCR_006646
Picard v2.8.0	Broad Institute	http://broadinstitute.github.io/picard ; RRID:SCR_006525
Trimmomatic v0.36	Bolger et al., 2014	http://www.usadellab.org/cms/?page=trimmomatic ; RRID:SCR_011848
GREAT	McLean et al., 2010	http://great.stanford.edu/public/html/ ; RRID:SCR_005807
ngsplot v2.63	Shen et al., 2014	https://github.com/shenlab-sinai/ngsplot ; RRID:SCR_011795
LOLA v1.12.0	Sheffield and Bock, 2016	https://bioconductor.org/packages/release/bioc/html/LOLA.html
HOMER v4.9	Heinz et al., 2010	http://homer.ucsd.edu/homer/ ; RRID:SCR_010881
deepTools v2.5.3	Ramirez et al., 2016	https://deeptools.readthedocs.io/en/develop/content/api.html ; RRID:SCR_016366
edgeR v3.12.1	Robinson et al., 2010	https://bioconductor.org/packages/release/bioc/html/edgeR.html ; RRID:SCR_012802
Metascape	Tripathi et al., 2015	http://metascape.org/gp/index.html#/main/step1 ; RRID:SCR_016620
UCSC Utilities	Kuhn et al., 2013	http://hgdownload.soe.ucsc.edu/downloads.html#utilities_downloads
SAMtools v0.1.19	Li et al., 2009	http://samtools.sourceforge.net/ ; RRID:SCR_002105

REAGENT or RESOURCE	SOURCE	IDENTIFIER
ChIPpeakAnno v3.17.0	Zhu et al., 2010	https://bioconductor.org/packages/release/bioc/html/ChIPpeakAnno.html ; RRID:SCR_012828
Principal components analysis (PCA)	Schafer and Strimmer, 2005/ Opgen-Rhein and Strimmer, 2007	http://www.strimmerlab.org/software/corpcor/
ZDOCK Server v.3.0.2	Pierce et al., 2014	http://zdock.umassmed.edu/
FloJo software v.10.4.1	TreeStar	https://www.flowjo.com
ConSurf Database	Ashkenazy et al., 2016	https://consurf.tau.ac.il/; RRID:SCR_002320
CYANA software	Guntert et al., 2009	www.cyana.org; RRID:SCR_014229
TALOS+ Sofware	Shen et al., 2009	N/A
NMRPipe	Delaglio et al., 19995	https://www.ibbr.umd.edu/nmrpipe/install.html
Iterative Soft Thresholding (istHMS)	Hyberts et al., 2012	N/A
CARA	Keller et al., 2004	http://www.cara.nmr.ch/doku.php
SonoLab Software	Covaris	http://covaris.com/instruments/sonolab-software/ ; RRID:SCR_016302
Integrative Genomics Viewer (IGV)	Broad Institute	http://www.broadinstitute.org/igv/ ; RRID:SCR_011793
HCS Studio Cell Analysis Software	Thermo Fisher Scientific	RRID:SCR_016787
Image Studio Lite	LI-COR	http://www.licor.com/bio/products/software/image_studio_lite/ ; RRID:SCR_013715
Geneious Prime v.2019.0.3	Geneious	http://www.geneious.com/; RRID:SCR_010519
Other		
Odyssey CLx Imaging System	LI-COR	RRID:SCR_014579
NextSeq 500 Sequencing System	Illumina	RRID:SCR_014983
NovaSeq 6000 Sequencing System	Illumina	RRID:SCR_016387
2200 TapeStation Instrument	Agilent	RRID:SCR_014994
E220 focused-ultrasonicator	Covaris	N/A
AKTA Pure chromatography system	GE Healthcare	N/A
700 MHz Agilent DD2 NMR Spectrometer equipped with a cryogenic probe	Agilent	N/A
ImageXpress Micro Confocal High Content Imaging System	Molecular Devices	N/A
Arrayscan XTI	Thermo Fisher Scientific	N/A
Aviv Model 430 CD spectrometer	Aviv Biomedical Inc.	N/A
Advantec Grade QR200 Quartz Fiber Filters	Cole-Parmer	EW-06658-10
Epson-Perfection V600 Photo Scanner	Epson	Model: B11B198011
NuPage 4-12% Bis-Tris gels, 12 and 15 well	Thermo Fisher Scientific/Invitrogen	Cat# NP0322BOX Cat# NP0336BOX

REAGENT or RESOURCE	SOURCE	IDENTIFIER
Novex 8% TBE gels, 15 well	Thermo Fisher Scientific/Invitrogen	Cat# EC62155BOX
Novex 10-20% Tricine gels	Thermo Fisher Scientific/Invitrogen	Cat# EC66252BOX
DNA Retardation Gels (6%)	Thermo Fisher Scientific/Invitrogen	Cat# EC63655BOX
Immobilon-FL PVDF membrane	EMD Millipore	Cat# 05317
Immobilon-PSQ PVDF membrane	EMD Millipore	Cat# ISEQ00010
Amicon Ultra-15 Centrifugal Filter Unit (30KDa MWCO)	EMD Millipore	Cat# UFC903024
Slide-A-Lyzer MINI dialysis unit (10 kDa MWCO)	Thermo Fisher Scientific	Cat# 69570
Slide-A-Lyzer MINI dialysis unit (3.5 kDa MWCO)	Thermo Fisher Scientific	Cat# 69550
Pierce Peptide Desalting Spin Columns	Thermo Fisher Scientific	Cat# 89851